THESIS FOR THE DEGREE OF DOCTOR OF PHILOSOPHY

Kinetic modeling of runaway-electron dynamics in partially ionized plasmas

LINNEA HESSLOW

Department of Physics
CHALMERS UNIVERSITY OF TECHNOLOGY
Göteborg, Sweden, 2020

Kinetic modeling of runaway-electron dynamics in partially ionized plasmas
LINNEA HESSLOW
ISBN 978-91-7905-243-0

Doktorsavhandlingar vid Chalmers tekniska högskola
Ny serie nr 4710
ISSN 0346-718X

Department of Physics
Chalmers University of Technology
SE–412 96 Göteborg
Sweden
Telephone +46 (0)31 772 1000

Cover:
The avalanche multiplication factor – the maximum amplification of a runaway seed – plotted as a function of deuterium and impurity densities. The color scale ranges from 10^{10} (black) to 10^{45} (white). The four panels show argon and neon impurities at temperatures of 5 eV and 10 eV.

Printed in Sweden by
Reproservice
Chalmers Tekniska Högskola
Göteborg, Sweden, 2020

Kinetic modeling of runaway-electron dynamics in partially ionized plasmas

LINNEA HESSLOW
Department of Physics
Chalmers University of Technology

Abstract

An essential result of kinetic plasma physics is the runaway phenomenon, whereby a fraction of an electron population can be accelerated to relativistic energies. Such runaway electrons are formed in astrophysical settings, but are also of great practical relevance to fusion research. In the most developed fusion device, known as the tokamak, runaway electrons have the potential to cause severe damage to the first wall. Runaway-electron mitigation is therefore one of the critical issues in the design of a fusion power plant.

In many situations, runaway electrons interact with partially ionized atoms. In particular, the currently envisaged mitigation method for tokamaks is to inject heavy atoms which collisionally dissipate the runaway beam before it can collide with the wall, or prevent it from forming at all. When the atoms are partially ionized, their bound electrons screen out a fraction of the atomic charge, which directly affects the collisional scattering rates. However, accurate expressions for these collisional scattering rates between energetic electrons and partially ionized atoms have not been available previously.

In this thesis, we explore kinetic aspects of runaway dynamics in partially ionized plasmas. We derive collisional scattering rates using a quantum-mechanical treatment, and study the interaction between fast electrons and partially ionized atoms. We then apply these results to calculate the threshold field for runaway generation, as well as the production rate of runaway electrons via the avalanche and Dreicer mechanisms. We find that even if material injection increases the dissipation rates, it also enhances avalanche generation which could potentially aggravate the runaway problem. These results contribute to more accurate runaway-electron modeling and can lead to more effective mitigation schemes in the longer term.

Keywords: plasma physics, Fokker–Planck equation, magnetic confinement fusion, tokamaks, runaway electrons, electron-ion collisions

Publications

This thesis is based on the following appended publications:

A L. Hesslow, O. Embréus, A. Stahl, T.C. DuBois, G. Papp, S.L. Newton and T. Fülöp,
Effect of partially screened nuclei on fast-electron dynamics,
Physical Review Letters **118**, 255001 (2017).
https://doi.org/10.1103/PhysRevLett.118.255001

B L. Hesslow, O. Embréus, M. Hoppe, T.C. DuBois, G. Papp, M. Rahm and T. Fülöp,
Generalized collision operator for fast electrons interacting with partially ionized impurities,
Journal of Plasma Physics **84**, 905840605 (2018).
https://doi.org/10.1017/S0022377818001113

C L. Hesslow, O. Embréus, G.J. Wilkie, G. Papp and T. Fülöp,
Effect of partially ionized impurities and radiation on the effective critical electric field for runaway generation,
Plasma Physics and Controlled Fusion **60**, 074010 (2018).
https://doi.org/10.1088/1361-6587/aac33e

D L. Hesslow, O. Embréus, O. Vallhagen and T. Fülöp,
Influence of massive material injection on avalanche runaway generation during tokamak disruptions,
Nuclear Fusion **59**, 084004 (2019).
https://doi.org/10.1088/1741-4326/ab26c2

E L. Hesslow, L. Unnerfelt, O. Vallhagen, O. Embreus, M. Hoppe, G. Papp and T. Fülöp,
Evaluation of the Dreicer runaway generation rate in the presence of high-Z impurities using a neural network,
Journal of Plasma Physics **85**, 475850601 (2019).
https://doi.org/10.1017/S0022377819000874

Statement of contribution

Paper A: I was the main person responsible for obtaining and analyzing the results, but worked in close collaboration with O. Embreus. I derived all the new equations, performed the numerical calculations and produced the figures. I wrote the manuscript together with the co-authors.

Paper B: I was the main person responsible for obtaining and analyzing the results, but worked in close collaboration with O. Embreus. I derived all equations except for those in section 4 and appendix B. I performed the numerical calculations and produced the figures, except for the calculation and production of figure 10. Apart from the conclusions, I drafted the entire manuscript, which was finalized together with the co-authors.

Paper C: I derived all the new equations, performed the numerical calculations and produced the figures. I and O. Embreus analyzed the results together. I wrote the draft of all sections but the introduction and conclusion, and finalized the paper with co-authors.

Paper D: I derived the main results (equation (9) and onward). I also performed the numerical calculations related to figure 2, and produced this figure. O. Embreus and I were equally involved in analyzing the results and writing the paper, which was finalized with input from co-authors.

Paper E: I was responsible for the methods used in the paper and supervised L. Unnerfelt who constructed the neural network as an undergraduate research project. I was the main author of the manuscript, and wrote all of section 2 and the appendices. I also performed the numerical calculations for section 2, and produced figures 1, 4 and 5.

Related publications, not included in the thesis

F L. Hesslow, O. Embréus, G.J. Wilkie, T.C. DuBois, G. Papp and T. Fülöp,
Fast-electron dynamics in the presence of weakly ionized impurities,
Europhysics Conference Abstracts **41F**, O4.118 (2017).
`http://ocs.ciemat.es/EPS2017PAP/pdf/O4.118.pdf`

G O. Embréus, L. Hesslow, M. Hoppe, G. Papp, K. Richards and T. Fülöp,
Dynamics of positrons during relativistic electron runaway,
Journal of Plasma Physics **84**, 905840506 (2019).
`https://doi.org/10.1017/S0022377818001010`

H O. Embréus, L. Hesslow, M. Hoppe, G. Papp, K. Richards and T. Fülöp,
Dynamics of positrons during relativistic electron runaway,
Europhysics Conference Abstracts **42A**, P5.4011 (2018).
`http://ocs.ciemat.es/EPS2018Pap/pdf/P5.4011.pdf`

I T. Fülöp, P. Helander, O. Vallhagen, O. Embreus, L. Hesslow, P. Svensson, A.J. Creely, N.T. Howard and P. Rodriguez-Fernandez,
Effect of plasma elongation on current dynamics during tokamak disruptions,
Journal of Plasma Physics **86**, 474860101 (2020).
`http://doi.org/10.1017/S002237782000001X`

J K. Insulander Björk, G. Papp, O. Embreus, L. Hesslow, T. Fülöp, O. Vallhagen, A. Lier, G. Pautasso, A. Bock, the ASDEX Upgrade Team and the EUROfusion MST1 Team,
Kinetic modelling of runaway electron generation in argon-induced disruptions in ASDEX Upgrade,
Accepted for publication in Journal of Plasma Physics (2020).
`https://arxiv.org/abs/2005.01606`

K O. Vallhagen, O. Embreus, I. Pusztai, L. Hesslow and T. Fülöp,
Runaway dynamics in ITER-like disruptions in the presence of massive material injection,
Accepted for publication in Journal of Plasma Physics (2020).
`https://arxiv.org/abs/2004.12861`

L M. Hoppe, L. Hesslow, O. Embreus, L. Unnerfelt, G. Papp, I. Pusztai, T. Fülöp, O. Lexell, T. Lunt, E. Macusova, P. J. McCarthy, G. Pautasso, G. I. Pokol, G. Por, P. Svensson, the ASDEX Upgrade team and the EUROfusion MST1 team, *Spatiotemporal analysis of the runaway distribution function from synchrotron images in an ASDEX Upgrade disruption*, Submitted to Journal of Plasma Physics (2020). `https://arxiv.org/abs/2005.14593`

M R. Sweeney, A.J. Creely, J. Doody, T. Fülöp, D.T. Garnier, R. Granetz, M. Greenwald, L. Hesslow, J. Irby, V.A. Izzo, R.J. La Haye, N.C. Logan, K. Montes, C. Paz-Soldan, C. Rea, R.A. Tinguely, O. Vallhagen and J. Zhu, *MHD Stability and Disruptions in the SPARC Tokamak*, Submitted to Journal of Plasma Physics (2020).

Acknowledgments

The last four years have been transformative for me. During my doctoral studies, I have truly appreciated learning fusion plasma physics and studying the equations governing the behavior of runaway electrons. But the most important reason for enjoying my time here is, of course, the people: *the academic family.*

As my supervisor, Professor Tünde Fülöp is my academic mother. Tünde takes all her students under her wings and makes great efforts to help us find a place in the academic environment. I deeply appreciate how Tünde has taught me paper writing, science strategies and shared many amusing anecdotes of academic life. I am also grateful to my academic godmother (co-supervisor) Sarah Newton, who is extraordinarily kind and always has time for questions and proof reading. Playing with my academic siblings Ola Embreus and Mathias Hoppe (i.e. discussing physics) is always exciting and intriguing. My academic big brother Gergely Papp has corrected many details of my manuscripts and showed me around when visiting tokamak experiments. With my room mate and academic nephew Andréas Sundström, there is always an interesting political or philosophical discussion. Finally, the entire plasma theory family have brought a sense of community and many cultural insights.

But even more important is the non-academic family. To my own little family, with my heart full of love: Markus and Vide, I am forever grateful for having you in my life.

Linnea Hesslow, Göteborg, May 2020

Contents

Chapter 1

Introduction

The possibility of a power plant that takes its fuel from ordinary sea water has created a great interest in fusion energy since the middle of the last century. Today, the prospect of a safe, CO_2-free and non-intermittent power source adds to the attractiveness of fusion. Although commercial fusion will likely be available too late to tackle climate change, it may play an important role in meeting the increasing energy demands during the later half of this century (Cabal *et al.*, 2017). Such a scenario however relies on functional power plants being available in approximately 50 years, and is sensitive to the policy support for fission as well as the cost and availability of carbon capture and storage technologies.

Considering the remarkable development of fusion during the last 50 years, there are reasons to be hopeful that fusion can indeed be achieved during the coming 50 years. For example, one of the most commonly adopted performance measures – the *triple product* – has increased by four orders of magnitude (CEA, 2016). This performance increase was achieved in the currently most developed fusion device known as the *tokamak*: a ring-shaped magnetic cage where the particles are confined by a twisted magnetic field. But fusion has also encountered unforeseen challenges which are not yet satisfactorily solved.

One such challenge is that posed by *runaway electrons*. In the undesired event of a plasma-terminating *disruption*, the tokamak can turn into a racetrack where electrons make millions of laps per second while they are accelerated by an electric field. If the resulting beam of relativistic

electrons hits the tokamak wall, it can locally melt significant amounts of the wall material (Matthews *et al.*, 2016). The potential for damage in such an event is so large that not a single unmitigated runaway electron event is allowed in future, larger tokamak devices operating with multi-MA plasma currents, such as ITER (Lehnen *et al.*, 2015). It is therefore essential to further develop runaway mitigation schemes, which requires accurate modeling of runaway-electron dynamics.

The runaway phenomenon is a basic result of plasma physics, and occurs in several contexts. The collisional friction force experienced by a fast plasma particle *decreases* with speed, so an electric field above a certain threshold – the *critical electric field* E_c – can accelerate particles to relativistic energies. This phenomenon is rather counterintuitive; translated into our every-day language, it would correspond to a drag force that decreased with velocity, resulting in an ever-increasing speed when cycling with a constant force on the pedals. The runaway mechanism will occur in plasmas with electric fields above the critical field E_c (Connor & Hastie, 1975), which includes several plasma systems: magnetic fusion devices (Helander *et al.*, 2002), astrophysical plasmas (Holman, 1985), and in lightning initiation where this mechanism is believed to play a key role (Dwyer, 2007; Lehtinen *et al.*, 1999).

In many plasmas where runaway electrons are observed, the runaway electrons interact with weakly ionized or neutral atoms. These *impurities* may be either atmospheric molecules, or the ions which are typically used to mitigate runaway electrons in magnetic fusion. Interaction with such impurities can drastically affect the dynamics of runaway electrons. If a slow electron interacts with a partially ionized ion, the interaction strength depends only on the net charge of the ion since the nucleus is *completely screened* by the bound electrons. In contrast, a fast electron can penetrate this cloud of bound electrons, which leads to *partial screening* of the nucleus. Since the interaction strength strongly depends on the degree of screening, this phenomenon has a significant impact on the runaway-electron dynamics. However, treatments of screening have previously been limited to simplified models, which either neglect quantum-mechanical effects (Martín-Solís *et al.*, 2015; Mosher, 1975), or employ the approximate Thomas–Fermi theory to calculate the density of bound electrons around the ions (Kirillov *et al.*, 1975; Zhogolev & Konovalov, 2014).

In this thesis, we derive a more accurate collision operator for fast electrons in partially ionized plasmas. In Papers A and B, we employ density functional theory (DFT) simulations to obtain accurate quantum-mechanical scattering cross-sections, from which we construct an analytical model for the collision operator. Furthermore, we implement this model in a kinetic solver for the electron distribution function, and study the effects of screening on runaway dynamics. Papers C-E apply this collision operator to investigate various aspects of runaway dynamics in the presence of partially ionized impurities, namely the effect on the threshold electric field (Paper C) and the steady-state runaway growth rates due to large-angle collisions (the avalanche mechanism; Paper D) as well as small-angle collisions (the Dreicer mechanism; Paper E). The presented model for collisions between fast electrons and partially ionized impurities represents the main contribution of this thesis and is applicable in and beyond tokamak research. Nevertheless, the primary application in mind is to runaways in tokamaks; in particular, some results in Papers C and D are specific to such scenarios. To put the contributions of this thesis into perspective, we now review the main mechanisms for runaway generation in tokamaks and the issues present in runaway modeling.

1.1 Generation of runaway electrons in tokamak experiments

Among systems which can sustain sufficiently large electric fields for runaway acceleration, the tokamak plasma is distinguished by its large inductance and its toroidal current. Both of these properties are closely linked to the formation of a large electric field in the tokamak.

Fortunately, the electric field required to produce the usual operational toroidal plasma current in a tokamak is generally below E_c, which means that runaway electrons are seldom observed during normal operation (Helander *et al.*, 2002). This is because the conductivity $\sigma \propto T^{3/2}$ is sufficiently large at high plasma temperatures that the toroidal current $I = \sigma A E$ (where A is the cross-section area) is large even at a low external electric field $E_\mathrm{ext} \ll E_\mathrm{c} \propto n$, where n is the electron density. Consequently, either a lower density or a decreased temperature (at a fixed plasma current) is required to obtain super-critical electric fields

and generate runaways. This corresponds to two different scenarios: low-density discharges and tokamak disruptions.

For runaway generation at low plasma density, the externally applied, current-driving electric field E_{ext} must exceed the critical electric field E_{c}, i.e. $E_{\text{ext}}/E_{\text{c}} \propto 1/(T^{3/2}n)$ must be sufficiently large. This condition is most easily achieved during tokamak start-up, where a larger electric field is applied to achieve plasma break-down and current ramp-up. In the early years of tokamak research, runaway electrons were routinely generated during the start-up phase (Knoepfel & Spong, 1979), but in today's experiments, runaway generation during this phase can be reduced by applying additional heating during ionization. In addition, any runaway seed population formed during current ramp-up can generally be suppressed by maintaining larger plasma densities (Granetz *et al.*, 2014). Consequently, runaway electrons are now only rarely observed during tokamak start-up, although some concern has recently been raised in this regard for ITER (de Vries & Gribov, 2018).

It is more difficult to prevent runaway generation during a disruption, which is an off-normal event where the plasma energy is suddenly lost, typically due to instabilities, in what is known as a *thermal quench* (TQ) (Hender *et al.*, 2007; de Vries *et al.*, 2011; Wesson, 2011; Wesson *et al.*, 1989). This temperature drop can decrease the conductivity $\sigma \propto T^{3/2}$ by several orders of magnitude, causing a *current quench* (CQ), which in turn induces an electric field $E_{\text{ind}} \propto -dI/dt$ (where I is the plasma current). The induced electric field can often drastically exceed the critical electric field and may convert a significant fraction of the initial plasma current into a runaway beam of several hundred kiloamperes (Hollmann *et al.*, 2015*a*). The numbers are even more dramatic in larger tokamaks such as ITER, with potential runaway currents of several megaamperes (Martín-Solís *et al.*, 2017; Paper K).

The potential runaway-electron damage increases with the size of the device. The main reason is that the internal magnetic energy in the plasma scales as $W_{\text{mag}} \propto I^2 R$ (where R is the major radius of the tokamak), and it is this energy that is partially converted into kinetic and magnetic energy of the runaway beam. Moreover, large devices confine high-energy particles better than small devices, which allows the electrons to reach higher energies before they are lost to the wall (Guan *et al.*, 2010; Knoepfel & Spong, 1979). Accordingly, runaway electrons are generally tolerable in today's tokamaks, whereas they will be un-

acceptable in larger reactor-size devices due to the risk of damage. In today's tokamaks, runaway electrons are therefore predominantly generated intentionally in dedicated experiments in order to develop reliable methods for runaway avoidance and mitigation. In these experiments, runaway electrons are usually created by either a disruption-causing impurity injection (Hollmann *et al.*, 2013), or by ramping up the current while constraining the density (or deacreasing the density at fixed current) until the electric field exceeds the critical field (Esposito *et al.*, 2003).

Runaway generation is more problematic for future devices not only because of the increased possible damage, but also since a runaway beam is more easily formed. The reason is intrinsic to kinetic theory of plasmas: the runaway density can increase exponentially with time in an *avalanche* created by large-angle collisions between runaway electrons and slower electrons. While the plasma current in present machines allows for some avalanche multiplication, this effect could amplify a small runaway seed by a devastating factor of $\sim 10^{20}$ in ITER (Rosenbluth & Putvinski, 1997). Experiments in small devices can therefore not investigate all aspects of the runaway problem in larger devices, which makes modeling crucial.

1.2 Runaway avoidance and mitigation

As for many other issues, prevention is better than cure when it comes to runaway damage mitigation. This means that the first line of defense is to avoid disruptions altogether. However, the mechanisms behind disruptions are only partially understood. It is widely known that there are limits on the maximum density, current and plasma β (the average ratio of the plasma pressure over the magnetic field pressure) beyond which major MHD instabilities are triggered (Freidberg, 2007). Disruptions do however also happen during operation within the safe regions of these limits, in which case the precise underlying mechanisms are not completely known. To better predict such disruptions, there are both physics-based and statistical approaches (Pautasso *et al.*, 2018). While the former approach aims to better understand the formation of certain instabilities in the plasma, the latter utilizes the large number of available tokamak pulses, often employing machine learning techniques (Cannas *et al.*, 2010; Kates-Harbeck *et al.*, 2019; Rattá *et al.*, 2010;

Wroblewski *et al.*, 1997). A drawback with this method is that the algorithms do not necessarily generalize well beyond the region where they were trained, such as to future, larger tokamaks. One may therefore expect that the first of these larger tokamaks will experience some disruptions, at least in the early phase of operation.

In the case where a disruption is approaching, and the control system fails to recover the plasma into a region of safe operation, the disruption mitigation system should be triggered and safely shut down the plasma (Lehnen *et al.*, 2015). The task of the disruption mitigation system is three-fold (Hollmann *et al.*, 2011*a*):

(i) to distribute the heat load in order to prevent melting of the plasma-facing components;

(ii) to limit the forces from currents induced in the vessel structures;

(iii) to suppress, or at least mitigate, runaway electrons.

Of the tokamaks where a disruption could seriously damage the wall, ITER is the closest to operation, and its disruption mitigation system represents the state of the art. Below, we therefore use ITER as an example, noting that the overall picture applies to other large tokamaks as well.

In ITER, the first two goals of the disruption mitigation system will be addressed by massive material injection, most likely in the form of shattered pellets of deuterium in combination with neon or argon (Pautasso *et al.*, 2018). The injected material will cause a thermal quench, in which approximately 90-95 % of the thermal and magnetic energy must be radiated to prevent wall melting (Hollmann *et al.*, 2015*b*; Lehnen *et al.*, 2015). Assuming sufficient material assimilation, this goal is realistic and can routinely be achieved in current experiments (Hollmann *et al.*, 2015*b*).

In order to limit the forces associated with induced currents, the current quench must be slow enough to prevent excessive eddy currents from being induced in the vessel. At the same time, the current quench must be sufficiently fast to ensure that the current has decayed considerably before the plasma strikes the vessel wall, driving halo currents (Hollmann *et al.*, 2011*a*). To reach these goals, the ITER target current quench time is in the interval 50-150 ms (Hollmann *et al.*, 2015*b*). This requirement

can also be fulfilled, provided there is enough assimilation of injected material.

However, it remains uncertain whether sufficient impurity quantities can be assimilated in ITER, and there is experimental evidence of poor impurity penetration into the plasma (Nardon *et al.*, 2016; Reux *et al.*, 2015). It is crucial that the impurity assimilation is sufficiently quick, otherwise the fraction of radiated energy during the thermal quench will be too low. In order to minimize the impurity delivery time as well as maximize the penetration depth into the plasma, the ITER disruption mitigation system will utilize shattered pellets (Breizman *et al.*, 2019; Commaux *et al.*, 2016). These pellets must contain a large amount of material compared to the original content in the plasma, but the required amount is modest in everyday life units: a few pellets of the size of a wine cork spread over the ITER volume of $830\,\mathrm{m}^{-3}$ would be enough for the impurity density to vastly exceed the original pre-injection density of the plasma (Breizman *et al.*, 2019).

The aim is that the injected material will not only mitigate the thermal and current quench loads, but also prevent runaway electron damage according to task (iii) above. As the main source of damage is localized wall melting if a runaway beam hits the wall, the maximum allowable runaway current is approximately 0.3-1.9 MA depending on the spatial distribution of the deposited material (Breizman *et al.*, 2019). The most straightforward means of reaching this goal is to prevent runaway formation by ensuring that the injected density is large enough that $E < E_\mathrm{c}$ at all times. This however requires the assimilated density to be larger than currently achieved in any experiment, and may therefore be unfeasible (Pautasso *et al.*, 2018). For this reason, a second material injection has been proposed for ITER, which would increase the runaway current decay rate. However, more recent simulations of so-called vertical displacement events show that a second impurity injection might accelerate the drift into the wall, in practice not affecting the magnitude of the current at wall strike, which implies that a faster current quench is not necessarily beneficial (Konovalov *et al.*, 2016; Pautasso *et al.*, 2018).

As the reliability of runaway mitigation and prevention by massive material injection is uncertain, alternative schemes have also been proposed. One suggested method is to use magnetic perturbations, either externally applied (Papp *et al.*, 2015*a*) or passively generated through the

design of the tokamak wall (Smith *et al.*, 2013), but these studies indicated that neither method is powerful enough for runaway prevention. It has also been studied whether wave-particle instabilities can suppress any runaway formation (Breizman & Aleynikov, 2017; Fülöp & Newton, 2014; Liu *et al.*, 2018; Pokol *et al.*, 2014), but again there is a lack of evidence for the efficacy of this method in ITER-like scenarios (Breizman *et al.*, 2019). For this reason, a number of alternative mitigation schemes are currently studied through a combination of experiment and modeling.

1.3 Modeling of runaway electrons in tokamaks

Realistic modeling and prediction of runaway-electron dynamics requires many different processes to be accounted for. Of these processes, momentum-space effects are among the most important and include collisions, radiation reaction as well as acceleration by the electric field. These processes, in turn, depend on the spatiotemporal evolution of the background plasma: the electric field determines the acceleration, the temperature and the plasma composition affect the collision rates, and breakup of magnetic surfaces gives rise to particle transport. A large runaway population may also lead to back-reaction on the induced electric field as well as the plasma ionization.

The multidimensional nature of the runaway problem – in combination with the wide separation in energy and time scale between thermal and relativistic particles – makes it computationally unfeasible to simultaneously model all the relevant effects accurately, which motivates the use of approximate methods. One such method is *reduced kinetic modeling*, also known as *runaway fluid modeling*, where kinetically determined runaway generation rates are implemented in tools which determine the background plasma evolution to varying degrees of sophistication (Fehér *et al.*, 2011; Helander *et al.*, 2002; Martín-Solís *et al.*, 2017; Papp *et al.*, 2013; Putvinski *et al.*, 1997; Smith *et al.*, 2006). However, as we further discuss in chapter 4, the available formulas for runaway generation were (prior to this thesis) inaccurate, and the description of transport is simplified in these models. Furthermore, the validity of reduced kinetic models has not been investigated systematically. To address these weaknesses, more idealized models can be useful to characterize and qualitatively understand the specific effects.

An example of a more idealized model is a pure momentum-space description, which is useful to study kinetic effects. This is the approach we take to explore the effect of partial screening on runaway dynamics in Papers A-C. In making the connection to a tokamak, this spatially homogeneous approach amounts to assuming that the runaway electrons are located close to the magnetic axis (the circle at the center of the torus), and neglecting their radial transport as well as the spatial variation of the electromagnetic fields. The momentum-space model is sophisticated enough to capture many features of runaway dynamics while being simple enough for extensive analytical and numerical analysis, which enabled us to develop an intuition about the relative importance of competing effects in different parameter regimes. The same approach has also been used to study radiation reaction (Embréus *et al.*, 2016; Stahl *et al.*, 2015), avalanche generation (Embréus *et al.*, 2018; Stahl *et al.*, 2016) and non-linear collisional effects (Stahl *et al.*, 2017).

Similarly, a suitable framework for studying runaway-electron transport in perturbed magnetic fields is to follow test particles in a prescribed magnetic field geometry, which can be obtained from, for example, magnetohydrodynamic (MHD) codes. This has been done in both magnetostatic fields, where the perturbations were generated by resonant magnetic perturbation coils (Papp *et al.*, 2012, 2015*a*; Särkimäki *et al.*, 2016), and in disruption scenarios involving massive material injection (Izzo *et al.*, 2011; Sommariva *et al.*, 2017).

Armed with the improved understanding from idealized models such as the examples above, it is possible to improve the reduced kinetic models. For example, more lightweight reduced kinetic models (which do not solve for the full MHD evolution) could be equipped with effective models of transport. To better account for partial screening, the runaway generation rates can be updated. In papers D and E, we thus approach a more quantitative description of runaway dynamics by improving reduced kinetic models.

1.4 Outline

In this thesis, we address the runaway interaction with an assumed background density of impurities. The model we develop is based on kinetic theory, which we therefore review in chapter 2, arriving at a kinetic equation for runaway electrons in a homogeneous plasma. In chapter 3, we use this kinetic equation to derive the basic runaway mechanisms and some key quantities. Chapter 4 takes a step towards experimental validation, and is focused on the reduced kinetic models introduced in section 1.3. Finally, chapter 5 highlights the main findings of the appended papers concerning the effect of screening on the dynamics of runaway electrons. We find strongly increased collision rates of runaway electrons compared to previous estimates. This effect increases both dissipation and avalanche rates, and therefore has promising as well as concerning implications for the potential to mitigate damaging runaway behavior in tokamaks.

Chapter 2

Kinetic theory for runaway electrons

The runaway phenomenon is fundamentally a kinetic effect depending on the balance between collisional friction and electric-field acceleration. Kinetic theory is therefore key to understanding runaway dynamics. Specifically, the collision operator is an essential object for the runaway mechanism and has a particularly important role in this thesis, which revolves around the collision operator in a partially ionized plasma. This chapter therefore presents an introduction to kinetic theory with particular emphasis on the collision operator. We then specialize the kinetic equation to an idealized momentum-space model for runaway electrons, and briefly introduce the numerical tool CODE (Landreman *et al.*, 2014; Stahl *et al.*, 2016), which has been used in all of the appended papers.

2.1 The kinetic equation

The kinetic equation determines the evolution of the probability distribution of particles in phase-space, and takes the form

$$\frac{\partial f_a}{\partial t} + \frac{\partial}{\partial \mathbf{z}} \cdot (\dot{\mathbf{z}} f_a) = C^a\{f_a\}. \tag{2.1}$$

Here, $f_a(\mathbf{x}, \mathbf{p}, t)$ is the distribution function of species a evaluated at time t, position $\mathbf{x}$ and momentum $\mathbf{p} = \gamma m \mathbf{v}$ (where $\gamma = 1/\sqrt{1 - v^2/c^2}$ is the

Lorentz factor and $\mathbf{v}$ is the velocity). The distribution is normalized so that the particle number density is given by $n_a(\mathbf{x}, t) = \int f_a(\mathbf{x}, \mathbf{p}, t)\, d^3p$. Moreover, $\partial/\partial\mathbf{z}$ denotes the gradient operator with respect to the phase-space coordinates $\mathbf{z} = (\mathbf{x}, \mathbf{p})$, and $\dot{\mathbf{z}} = (\mathbf{v}, \mathbf{F}_a)$ is the time derivative of $\mathbf{z}$. In a plasma, the force is given by $\mathbf{F}_a = q_a(\mathbf{E} + \mathbf{v} \times \mathbf{B})$, where $\mathbf{E}$ and $\mathbf{B}$ are the electric and magnetic fields respectively, and q_a is the charge of species a.

The distribution function f_a is a statistical object in the sense that it denotes a smooth function where the point-like contributions from individual particles have been ensemble averaged over many macroscopically equivalent particle configurations. Similarly, the forces acting on the distribution function are averaged, which removes the short-length-scale interaction between individual particles. This contribution to the dynamics is instead described by the collision operator $C^a\{f_a\} = \sum_b C^{ab}\{f_a, f_b\}$ on the right-hand side of the kinetic equation (2.1), which gives the time rate of change in f_a due to collisions with all species b in the plasma. When the collision operator is discussed in the following section and elsewhere, we will use the shorter notation $C^{ab} \equiv C^{ab}\{f_a, f_b\}$.

A rigorous derivation of the kinetic equation is outside the scope of the present text. Such derivation is associated with several subtle issues including precise definitions of the averaging process, particularly in the collision operator (Montgomery & Tidman, 1964). Nevertheless, the kinetic equation can be intuitively understood in a simple manner as a continuity equation with an additional term from the collision operator, which describes the effect of the microscopic fields. Without collisions, the distribution function would obey the continuity equation, i.e. $\partial f_a/\partial t + (\partial/\partial\mathbf{z}) \cdot (\dot{\mathbf{z}} f_a) = 0$. In a Hamiltonian system, this continuity equation leads to Liouville's theorem, stating that the distribution function is conserved along the trajectories of a system (Tong, 2012). With the dissipation introduced by collisions, the system is, however, no longer Hamiltonian which invalidates Liouville's theorem. As a consequence, the motion of individual particles is not deterministic, but can be described by a stochastic differential equation known as the Langevin equation (Tong, 2012).

2.2 The Fokker–Planck collision operator

The form of the collision operator depends on the range of the inter-particle forces, which significantly differs between neutral gases versus plasmas. Short-range forces decrease rapidly with inter-particle distance r, and include molecular forces which fall off as $1/r^6$ or $1/r^7$ (Montgomery & Tidman, 1964). This short-range interaction is dominated by large-angle two-body collisions, which are described by the Boltzmann collision operator. The Boltzmann operator can be understood as the rate at which species a scatters from $\mathbf{p}_1$ into $\mathbf{p}$, minus the rate of the opposite scattering process. Its general form is (Cercignani & Kremer, 2002)

$$C^{ab}_{\text{Boltz}} = \int \frac{d\sigma_{ab}}{d\Omega} g_{\text{ø}} \left[f_a(\mathbf{p}_1) f_b(\mathbf{p}_2) - f_a(\mathbf{p}) f_b(\mathbf{p}') \right] d^3p' d\Omega, \tag{2.2}$$

where $g_{\text{ø}} = \sqrt{(\mathbf{v} - \mathbf{v}')^2 - (\mathbf{v} \times \mathbf{v}')^2/c^2}$ is the Møller relative speed and $d\sigma_{ab}/d\Omega$ is the differential cross section for collisions in which the momentum of species a changes from $\mathbf{p}$ to $\mathbf{p}_1$, and $\mathbf{p}' \rightarrow \mathbf{p}_2$ for species b.

In contrast to gases of molecules, plasma particles mainly interact via long-range forces, namely Coulomb forces. Coulomb forces fall off as the inverse square of the inter-particle distance $1/r^2$. The distinguishing feature of inverse-square forces is that the interaction is dominated by small-angle deflections to the particle trajectories, which are described by the Fokker–Planck operator.

The Fokker–Planck operator may be obtained from a small-angle expansion of the Boltzmann operator but it can also be derived independently using methods from statistical mechanics (Montgomery & Tidman, 1964). The Fokker–Planck collision operator between species a and b is given by

$$C^{ab}_{\text{FP}} = -\nabla_k \left(f_a \langle \Delta p^k \rangle_{ab} \right) + \frac{1}{2} \nabla_k \nabla_l \left(f_a \langle \Delta p^k \Delta p^l \rangle_{ab} \right), \tag{2.3}$$

where the term $\langle \Delta p^k \rangle_{ab}$ represents the average rate of change in the kth component of the momentum of the incoming electron during a collision, while $\langle \Delta p^k \Delta p^l \rangle_{ab}$ describes the average rate of change in the tensor $p^k p^l$. Here, ∇_k refers to the momentum-space gradient operator.

These average momentum changes are given by

$$\begin{aligned}\left\langle \Delta p^k \right\rangle_{ab} &= \int d\mathbf{p}' f_b(\mathbf{p}') \int \frac{d\sigma_{ab}}{d\Omega} g_\phi \Delta p^k d\Omega, \\ \left\langle \Delta p^k \Delta p^l \right\rangle_{ab} &= \int d\mathbf{p}' f_b(\mathbf{p}') \int \frac{d\sigma_{ab}}{d\Omega} g_\phi \Delta p^k \Delta p^l d\Omega.\end{aligned} \tag{2.4}$$

The angular integrals in equations (2.4) are taken over

$$\int d\Omega = \int_{\theta_{\min}}^{\pi} \sin\theta \, d\theta \int_0^{2\pi} d\phi, \tag{2.5}$$

where $\theta_{\min}$ is the minimum scattering angle below which Debye shielding screens out long-range interaction. This shielding effect means that each plasma particle only interacts with particles within a distance of the Debye length λ_{D}; over larger distances, the plasma species will be distributed to ensure macroscopic charge neutrality.

Without the minimum angle $\theta_{\min}$, the integrals in the Fokker–Planck operator (2.3) would diverge, since the Coulomb-interaction cross section scales as $d\sigma_{ab}/d\Omega \propto \sin^{-4}(\theta/2)$ while the lowest-order terms in $\Delta p^k d\Omega$ and $\Delta p^k p^l d\Omega$ are of order $\sim \sin^3(\theta/2) d[\sin(\theta/2)]$ (Rosenbluth *et al.*, 1957). The collision operator thus acquires terms which are proportional to the *Coulomb logarithm* $\ln\Lambda = \ln(2/\theta_{\min})$, which is typically large in magnetic-fusion plasmas due to the large number of particles within a Debye sphere (Helander & Sigmar, 2005). The Coulomb logarithm quantifies the dominance of small-angle collisions over large-angle collisions, and thereby determines the validity of the Fokker–Planck operator. Since the Fokker–Planck operator can only model small-angle collisions accurately, it only contains the leading-order terms in $\ln\Lambda$. Unless the order-unity terms (i.e. $\ll \ln\Lambda$) can be neglected, the resulting operator will exhibit unphysical energy transfers between the different species. Such unphysical properties can also appear in the collision operator for partially ionized plasmas that we derive in this thesis, and are addressed in Paper B.

As for its numerical value, the Coulomb logarithm has an energy dependence which can be significant for particles with momentum much larger than the thermal speed, in particular if the temperature is low and the density is high. An expression for this energy-dependence can be obtained from matching the thermal Coulomb logarithm from Wesson (2011),

$$\ln\Lambda_0 = 14.9 - 0.5\ln(n_{\mathrm{e}}\,[10^{20}\,\mathrm{m}^{-3}]) + \ln(T\,[\mathrm{keV}]), \tag{2.6}$$

and the high-energy formula from Solodov & Betti (2008), according to

$$\begin{aligned} \ln\Lambda^{\mathrm{ee}} &= \ln\Lambda_0 + \frac{1}{k}\ln\left(1+\left[2(\gamma-1)/\bar{p}_{\mathrm{Te}}^2\right]^{k/2}\right), \\ \ln\Lambda^{\mathrm{ei}} &= \ln\Lambda_0 + \frac{1}{k}\ln\left[1+(2\bar{p}/\bar{p}_{\mathrm{Te}})^k\right], \end{aligned} \tag{2.7}$$

where "e" and "i" denotes electrons and ions respectively, $\bar{p} = p/(m_{\mathrm{e}}c)$ is the normalized momentum and $\bar{p}_{\mathrm{Te}} = \sqrt{2T_{\mathrm{e}}/(m_{\mathrm{e}}c^2)}$ is the normalized thermal momentum. In the appended papers, the parameter $k = 5$ was chosen to give a smooth transition between the thermal and the high-energy expressions.

For runaway electrons, the relation between the Fokker–Planck operator and the Boltzmann operator is more than a theoretical curiosity, since both are needed to model the runaway dynamics. In most magnetic-fusion plasmas, small-angle collisions dominate over large-angle collisions in which case the Fokker–Planck operator accurately models the dynamics. Small-angle collisions dominate also in runaway-prone plasmas, but here, large-angle collisions introduce a new runaway mechanism known as the avalanche effect, which causes an exponential growth of the runaway population. The Fokker–Planck and Boltzmann operators must therefore be combined to describe runaway dynamics.

Large-angle collisions are also enhanced in partially ionized plasmas, which could challenge the validity of the Fokker–Planck operator to model the effect of partial screening. In Paper B, we therefore investigate the validity pitch-angle scattering in the Fokker–Planck operator by comparing it to the Boltzmann operator. We find a negligible difference in key runaway quantities such as runaway density, current and generation rates, implying that the Fokker–Planck operator is adequate also in partially ionized plasmas for typical tokamak parameters.

2.2.1 Linearized collision operator

In highly collisional plasmas, including many tokamak scenarios and runaway events, the distribution is close to its thermal equilibrium, which in a relativistic plasma is given by the Maxwell–Jüttner distribution (the *Maxwellian* for short) (Cercignani & Kremer, 2002)

$$f_{\mathrm{Ma}}(\mathbf{p}) = \frac{n_a}{4\pi m_a^3 c^3 \Theta_a K_2(1/\Theta_a)} \exp\left(-\frac{\gamma}{\Theta_a}\right), \tag{2.8}$$

where $\Theta_a = T_a/(m_a c^2)$ is the temperature[1] of species a normalized to the rest energy and $K_2(1/\Theta_a)$ is the second-order modified Bessel function of the second kind. In the non-relativistic limit $\Theta \ll 1$, the Maxwell–Jüttner distribution simplifies to the Maxwell–Boltzmann distribution, which may be obtained by expanding equation (2.8) in small Θ, in which case $K_2(1/\Theta) \sim e^{-1/\Theta}\sqrt{\pi\Theta/2}$. The non-relativistic Maxwellian is accordingly given by (Helander & Sigmar, 2005)

$$f_{\mathrm{M}a}(\mathbf{p}) = \frac{n_a}{\pi^{3/2} m_a^3 v_{\mathrm{T}a}^3} \exp\left(-\frac{v^2}{v_{\mathrm{T}a}^2}\right), \tag{2.9}$$

where $v_{\mathrm{T}a} = \sqrt{2T_a/m_a}$ is the thermal speed.

If the distribution is close to its thermal equilibrium, the collision operator can be linearized around a Maxwellian. A linear collision operator can well describe many aspects of runaway dynamics. This is because many runaway scenarios have a trace runaway population, since even a small fraction of relativistic particles are enough to carry the full initial plasma current. Full current conversion sets the upper limit of the runaway current due to induction, and thereby restricts the maximum runaway density, if the average runaway speed is close to the speed of light. Two interesting exceptions where a linear operator may be inadequate are if the distribution is strongly distorted, or if the electric field is large, both of which may occur during tokamak disruptions. Such scenarios can not be modeled by the linear collision operator, but require a non-linear collision operator, such as that considered by Stahl *et al.* (2017), which was derived by Braams & Karney (1989).

The linearized Fokker–Planck collision operator consists of two pieces: the *test-particle* operator $C^{ab}_{\mathrm{FP,tp}}$ and the *field-particle* operator $C^{ab}_{\mathrm{FP,fp}}$. The test-particle operator describes how the perturbation to the Maxwellian is affected by collisions with the Maxwellian background, while the field-particle operator describes the back-reaction from the perturbation on the Maxwellian. As a concrete example, the friction on a runaway population is determined by the test-particle operator whereas the field-particle operator modifies the bulk population, which is needed to obtain the correct conductivity in the plasma. The test-particle operator thus contains the essential interaction for runaway physics.

[1] We follow the plasma-physics convention to include a factor of the Boltzmann constant k_{B} in the temperature, which gives it units of energy.

The test-particle operator for species a (2.3) can be parametrized by the three collision frequencies ν_{D}^{ab}, ν_{S}^{ab} and $\nu_{\parallel}^{ab}$ (Helander & Sigmar, 2005):

$$C_{\mathrm{FP,tp}}^{ab} = \nu_{\mathrm{D}}^{ab}\mathscr{L}\{f_a\} + \frac{1}{p^2}\frac{\partial}{\partial p}\left[p^3\left(\nu_{\mathrm{S}}^{ab} f_a + \frac{1}{2}\nu_{\parallel}^{ab} p\frac{\partial f_a}{\partial p}\right)\right], \tag{2.10}$$

where the Lorentz scattering operator

$$\mathscr{L} = \frac{1}{2}\left[\frac{1}{\sin\theta}\frac{\partial}{\partial\theta}\left(\sin\theta\frac{\partial}{\partial\theta}\right) + \frac{1}{\sin^2\theta}\frac{\partial^2}{\partial\phi^2}\right] \tag{2.11}$$

causes deflection at constant energy, known as pitch-angle scattering.

The processes described by the three collision frequencies in equation (2.10) drive the distribution f_a toward a Maxwellian distribution through different mechanisms. The deflection frequency ν_{D}^{ab} increases isotropy, and will counter-act any beam-like structures which can be generated by, for example, a large electric field. In the energy distribution, the slowing-down frequency ν_{S}^{ab} describes collisional friction, whereas the parallel momentum diffusion frequency $\nu_{\parallel}^{ab}$ reduces sharp gradients of the energy distribution. As a consequence of these collisional effects, a distribution in equilibrium is isotropic, and the balance between collisional friction and momentum diffusion gives the familiar bell shape of a Maxwellian.

The test-particle part of the electron collision operator is composed of the electron-electron and the electron-ion collision operator, where the latter only contains the pitch-angle scattering; in the limit of small electron-to-ion mass ratio, energy transfers between the two species are negligible. Accordingly, the test-particle electron collision operator takes the form

$$C_{\mathrm{FP,tp}}^{\mathrm{e}} = \left(\nu_{\mathrm{D}}^{\mathrm{ee}} + \nu_{\mathrm{D}}^{\mathrm{ei}}\right)\mathscr{L}\{f_{\mathrm{e}}\} + \frac{1}{p^2}\frac{\partial}{\partial p}\left[p^3\left(\nu_{\mathrm{S}}^{\mathrm{ee}} f_{\mathrm{e}} + \frac{1}{2}\nu_{\parallel}^{\mathrm{ee}} p\frac{\partial f_{\mathrm{e}}}{\partial p}\right)\right]. \tag{2.12}$$

In a fully ionized plasma (to be generalized in section 2.3), the collision frequencies are given by (Braams & Karney, 1989; Pike & Rose, 2014)[2]

[2] In equation (2.13), there is no energy-dependent Coulomb logarithm factor $\ln\Lambda^{\mathrm{ee}}/\ln\Lambda_0$ in $\nu_{\parallel}^{\mathrm{ee}}$. This is because such a factor would entail adding terms $\propto \partial\ln\Lambda^{\mathrm{ee}}(p)/\partial p$ to $\nu_{\mathrm{S}}^{\mathrm{ee}}$. However, the parallel diffusion frequency vanishes at superthermal momentum as shown in section 2.2.2, which implies that $\ln\Lambda^{\mathrm{ee}} \approx \ln\Lambda_0$ everywhere where $\nu_{\parallel}^{\mathrm{ee}}$ is non-negligible and thus justifies the approximation.

$$
\begin{aligned}
\nu_{\mathrm{S}}^{\mathrm{ee}} &= \frac{1}{\tau_{\mathrm{c}}}\frac{1}{\bar{p}}\frac{\ln\Lambda^{\mathrm{ee}}}{\ln\Lambda_0}\Psi_{\mathrm{S}}(\bar{p},\Theta),\\
\nu_{\parallel}^{\mathrm{ee}} &= \frac{1}{\tau_{\mathrm{c}}}\frac{2\gamma\Theta}{\bar{p}^3}\Psi_{\mathrm{S}}(\bar{p},\Theta),\\
\nu_{\mathrm{D}}^{\mathrm{ee}} &= \frac{1}{\tau_{\mathrm{c}}}\frac{2}{\bar{p}^2}\frac{\ln\Lambda^{\mathrm{ee}}}{\ln\Lambda_0}\Psi_{\mathrm{D}}(\bar{p},\Theta),\\
\nu_{\mathrm{D}}^{\mathrm{ei}} &= \frac{1}{\tau_{\mathrm{c}}}\frac{\gamma}{\bar{p}^3}\frac{\ln\Lambda^{\mathrm{ei}}}{\ln\Lambda_0}Z_{\mathrm{eff}}.
\end{aligned}
\tag{2.13}
$$

Here, $\Theta = T_{\mathrm{e}}/(m_{\mathrm{e}}c^2)$, $Z_{\mathrm{eff}} = \sum_j n_j Z_j^2/n_{\mathrm{e}}$ is the effective plasma charge,

$$
\tau_{\mathrm{c}} = \frac{4\pi\varepsilon_0^2 m_{\mathrm{e}}^2 c^3}{n_{\mathrm{e}} e^4 \ln\Lambda_0}
\tag{2.14}
$$

is a relativistic collision time, and the Coulomb logarithm is given in equation (2.7). The functions Ψ_{D} and Ψ_{S} take the form

$$
\begin{aligned}
\Psi_{\mathrm{S}}(\bar{p},\Theta) &= \frac{\gamma^2\Psi_1 - \Theta\Psi_0 + (\Theta\gamma - 1)\bar{p}e^{-\gamma/\Theta}}{\bar{p}^2 K_2(1/\Theta)},\\
\Psi_{\mathrm{D}}(\bar{p},\Theta) &= \frac{1}{2\gamma\bar{p}^3 K_2(1/\Theta)}\Big(\big(\bar{p}^2\gamma^2 + \Theta^2\big)\Psi_0 + \Theta\big(2\bar{p}^4 - 1\big)\Psi_1\\
&\quad +\gamma\Theta\big[1 + \Theta\big(2\bar{p}^2 - 1\big)\big]\bar{p}e^{-\gamma/\Theta}\Big),
\end{aligned}
\tag{2.15}
$$

where

$$
\begin{aligned}
\Psi_0 &= \int_0^{\bar{p}} \frac{1}{\sqrt{1+s^2}} \exp\left(-\sqrt{1+s^2}/\Theta\right) ds,\\
\Psi_1 &= \int_0^{\bar{p}} \exp\left(-\sqrt{1+s^2}/\Theta\right) ds,
\end{aligned}
\tag{2.16}
$$

and K_2 is the second-order modified Bessel function of the second kind.

2.2.2 Collision frequencies at non-relativistic temperatures

To elucidate the behavior of the collision frequencies presented in equation (2.13), we evaluate them at a non-relativistic temperature $\Theta \ll 1$ and in the limit of both non-relativistic momentum ($\bar{p} \ll 1$) and superthermal momentum ($\gamma - 1 \gg \Theta$).

In the non-relativistic temperature limit, $s \ll 1$ dominates the integrals (2.16) and we may approximate

$$\begin{aligned} \Psi_1, \Psi_0 \approx \Psi &\equiv e^{-1/\Theta} \int_0^{\bar{p}} e^{-s^2/2} ds = e^{-1/\Theta} \sqrt{\frac{\pi\Theta}{2}} \phi(x), \\ K_2(1/\Theta) &\approx e^{-1/\Theta} \sqrt{\pi\Theta/2}, \end{aligned} \tag{2.17}$$

where $\phi(x) = (2/\sqrt{\pi}) \int_0^x e^{-y^2} dy$ is the error function and we defined $x \equiv \bar{p}/\sqrt{2\Theta}$, which approaches v/v_{Te} for non-relativistic speeds.

For Ψ_{S}, we obtain the following in the superthermal and non-relativistic limits, respectively:

$$\begin{aligned} \Psi_{\mathrm{S}}(\bar{p}, \Theta) &\approx \frac{\gamma^2}{\bar{p}^2} \phi\left(x\right) - \frac{1}{\bar{p}^2} \sqrt{\frac{2}{\pi\Theta}} \bar{p} e^{-(\gamma-1)/\Theta} \\ &\to \begin{cases} \dfrac{\gamma^2}{\bar{p}^2}, & \gamma - 1 \gg \Theta, \\ G(x)/\Theta, & \bar{p} \ll 1, \end{cases} \end{aligned} \tag{2.18}$$

where $G(x)$ is the Chandrasekhar function

$$G(x) = \frac{\phi(x) - x\phi'(x)}{2x^2} \to \begin{cases} \frac{2x}{3\sqrt{\pi}}, & x \to 0 \\ \frac{1}{2x^2} & x \to \infty \end{cases}. \tag{2.19}$$

The Chandrasekhar function peaks at $x \approx 1$, and then monotonically decreases.

Similarly, for Ψ_{D},

$$\Psi_{\mathrm{D}}(\bar{p}, \Theta) \to \begin{cases} \frac{\gamma}{2\bar{p}}, & \gamma - 1 \gg \Theta, \\ \frac{1}{2\bar{p}} \underbrace{\left[\left(1 - \frac{\Theta}{\bar{p}^2}\right)\phi(x) - \frac{1}{\bar{p}}\sqrt{\frac{2\Theta}{\pi}} e^{-x^2}\right]}_{=\phi(x) - G(x)}, & \bar{p} \ll 1. \end{cases} \tag{2.20}$$

The collision frequencies in equation (2.13) thus take the following form in the non-relativistic limit:

$$\begin{aligned} \nu_{\mathrm{S}}^{\mathrm{ee}} &\to \frac{1}{\tau_{\mathrm{c}}} \frac{c}{v} \frac{\ln \Lambda^{\mathrm{ee}}}{\ln \Lambda_0} \frac{G(x)}{\Theta}, \\ \nu_{\parallel}^{\mathrm{ee}} &\to \frac{2}{\tau_{\mathrm{c}}} \frac{c^3}{v^3} G(x), \\ \nu_{\mathrm{D}} = (\nu_{\mathrm{D}}^{\mathrm{ee}} + \nu_{\mathrm{D}}^{\mathrm{ei}}) &\to \frac{1}{\tau_{\mathrm{c}}} \frac{c^3}{v^3} \left(\frac{\ln \Lambda^{\mathrm{ee}}}{\ln \Lambda_0} \left[\phi(x) - G(x)\right] + Z_{\mathrm{eff}} \frac{\ln \Lambda^{\mathrm{ei}}}{\ln \Lambda_0} \right), \end{aligned} \tag{2.21}$$

Likewise, the superthermal collision frequencies are, at a non-relativistic temperature, given by

$$\begin{aligned} \nu_{\mathrm{S}}^{\mathrm{ee}} &\to \frac{1}{\tau_{\mathrm{c}}}\frac{\gamma^2}{\bar{p}^3}\frac{\ln\Lambda^{\mathrm{ee}}}{\ln\Lambda_0}, \\ \nu_{\parallel}^{\mathrm{ee}} &\to 0, \\ \nu_{\mathrm{D}} &\to \frac{1}{\tau_{\mathrm{c}}}\frac{\gamma}{\bar{p}^3}\left(\frac{\ln\Lambda^{\mathrm{ee}}}{\ln\Lambda_0} + Z_{\mathrm{eff}}\frac{\ln\Lambda^{\mathrm{ei}}}{\ln\Lambda_0}\right). \end{aligned} \tag{2.22}$$

Several insights into runaway dynamics can be made almost directly from inspecting the collision frequencies in equations equations (2.21) and (2.22). As will be further discussed in chapter 3, the fact that $p\nu_{\mathrm{S}}^{\mathrm{ee}}$ decreases with speed above $x \approx 1$ gives rise to the runaway mechanism, and its behavior as $p \to \infty$ defines the threshold field for the runaway mechanism.

2.3 Collisions between electrons and partially ionized atoms

Fast electrons are strongly affected by interaction with partially ionized atoms. Unlike the case of a fully ionized plasma, the electron-ion interaction strength depends on the electron energy due to the energy-dependent screening of the N_{e} bound electrons around the ion; a low-energy electron will experience a *completely screened* ion with the net ion charge Z_0, whereas an ultrarelativistic electron will approach the limit of *no screening*, where the interaction strength is determined by the full nuclear charge Z. Moreover, the electron experiences an increasing rate of inelastic collisions with the bound electrons as its energy increases. Since the collision frequencies vary linearly with electron density, and the deflection frequency varies approximately quadratically with the ion charge, the collision rates for fast electrons are strongly enhanced in the presence of weakly ionized impurities, compared to when the nuclei are completely screened by the bound electrons.[3]

The collision operator between fast electrons and partially ionized atoms consists of two parts: collisions with the nuclei and collisions with the

[3]Throughout this thesis, we use the limit of complete screening as reference in expressions such as "*enhanced* dissipation rates".

bound electrons. In both cases, the target particle can be treated as stationary; ions have a lower velocity than electrons due to the small electron-to-ion mass ratio (assuming the electron and ion temperatures are of the same order of magnitude), and the bound electrons are slow since they would not be bound if their kinetic energy exceeded the binding energy. Collisions with partially ionized atoms will therefore only affect the test-particle part of the electron collision operator.

In the electron-ion collision operator $C^{\mathrm{ei}}_{\mathrm{FP,tp}}$, only $\nu^{\mathrm{ei}}_{\mathrm{D}}$ is modified by partial screening, since no energy transfer is kinematically allowed between ions and electrons in the limit of small electron-to-ion mass ratio. To calculate $\nu^{\mathrm{ei}}_{\mathrm{D}}$, we evaluate the collision operator (2.3) for stationary target particles. This derivation of the collision operator follows Rosenbluth *et al.* (1957) but the Rutherford cross-section is replaced by the quantum-mechanical cross section for collisions with bound electrons, taken in the Born approximation (Heitler, 1954; Landau & Lifshitz, 1958):

$$\frac{d\sigma_{\mathrm{e}j}}{d\Omega} = \frac{r_0^2}{4\bar{p}^4}\left(\frac{\cos^2(\theta/2)\bar{p}^2+1}{\sin^4(\theta/2)}\right)|Z_j - F_j(q)|^2\,. \tag{2.23}$$

Here, $r_0 = e^2/(4\pi\epsilon_0^2 m_{\mathrm{e}}c^2)$ is the classical electron radius and Z_j is the atomic number (the full nuclear charge) for ion species j. The form factor is defined as

$$F_j(\mathbf{q}) = \int \rho_{\mathrm{e},j}(r)\mathrm{e}^{-\mathrm{i}\mathbf{q}\cdot\mathbf{r}/a_0}\,d\mathbf{r}, \tag{2.24}$$

where a_0 is the Bohr radius, and $\mathbf{q} = 2\bar{\mathbf{p}}\sin(\theta/2)/\alpha$ with the fine-structure constant $\alpha \approx 1/137$. The electronic charge density of the ion is denoted $\rho_{\mathrm{e},j}(r)$, and must in general be determined by numerical methods such as density functional theory (DFT); see Paper B. By inspecting the form factor, the limits of complete screening and no screening can be identified. Complete screening is obtained as the exponential approaches unity at low q, which implies that $F_j \to N_{\mathrm{e},j}$ and $|Z_j - F_j|^2 \to Z_{0,j}^2$, where $N_{\mathrm{e},j}$ is the number of bound electrons and $Z_{0,j}$ is the charge number (the net charge) of the ion. Conversely, the no screening limit is approached at high q since the fast oscillations in the exponential cause the form factor to vanish, which yields $|Z_j - F_j|^2 \to Z_j^2$.

In Papers A and B, we developed an analytical expression for the partially screened deflection frequency. As we were mostly concerned with the behavior of the collision operator, the form of this expression was

chosen to ensure that $\nu_{\mathrm{D}}^{\mathrm{ei}}$ well captures the energy-dependence of the full DFT solution to the deflection frequency. In this regard, we found that a one-parameter model, which generalizes the expression by Kirillov *et al.* (1975), was sufficient. The free parameter was determined so that the high-energy asymptote of $\nu_{\mathrm{D}}^{\mathrm{ei}}$ exactly followed the DFT solution. This method gave an accurate model for the collision operator, but the model is less appropriate for processes with a different dependence on the form factor, such as bremsstrahlung radiation where a Yukawa-type potential is more suitable (Lamoureux & Avdonina, 1997).

With this model, $\nu_{\mathrm{D}}^{\mathrm{ei}}$ in equation (2.13) is modified according to

$$\nu_{\mathrm{D}}^{\mathrm{ei}} = \frac{1}{\tau_{\mathrm{c}}}\frac{\gamma}{\bar{p}^3}\frac{1}{\ln\Lambda_0}\left(\ln\Lambda^{\mathrm{ei}} Z_{\mathrm{eff}} + g(\bar{p})\right), \tag{2.25}$$

where the partial screening correction is

$$g(\bar{p}) = \sum_j \frac{n_j}{n_{\mathrm{e}}}\left\{\frac{2}{3}\left(Z_j^2 - Z_{0,j}^2\right)\ln\left[(\bar{p}\bar{a}_j)^{3/2}+1\right] - \frac{2}{3}\frac{N_{\mathrm{e},j}^2(\bar{p}\bar{a}_j)^{3/2}}{(\bar{p}\bar{a}_j)^{3/2}+1}\right\}. \tag{2.26}$$

The normalized length parameter $\bar{a}_j$ is determined from the density of bound electrons around the ion and is thus related to the ion radius. Its numerical values are given for some fusion-relevant elements in Paper B.

Regarding the electron-electron collision operator $C_{\mathrm{FP,tp}}^{\mathrm{ee}}$, we modify the slowing-down frequency $\nu_{\mathrm{S}}^{\mathrm{ee}}$ according to the Bethe stopping-power formula (Bethe, 1930; Jackson, 1999). No modification is however needed in $\nu_{\parallel}^{\mathrm{ee}}$; as shown in equation (2.22) it vanishes at superthermal electron momenta and is therefore adequately described by the completely screened expression, which is valid at thermal energies. We also neglect the effects in $\nu_{\mathrm{D}}^{\mathrm{ee}}$, since there is no analytic expression for the differential cross section for collisions with bound electrons. As discussed in Paper B, this approximation can be motivated by the fact that $\nu_{\mathrm{D}}^{\mathrm{ei}} \gg \nu_{\mathrm{D}}^{\mathrm{ee}}$ if the effects of screening are significant, and thus the total deflection frequency $\nu_{\mathrm{D}} = \nu_{\mathrm{D}}^{\mathrm{ei}} + \nu_{\mathrm{D}}^{\mathrm{ee}}$ is well approximated even with the completely-screened expression for $\nu_{\mathrm{D}}^{\mathrm{ee}}$. Conversely, if the screening effects are insignificant, the completely-screened expression will resemble $\nu_{\mathrm{D}}^{\mathrm{ee}}$ per definition.

The resulting, modified expression for $\nu_{\mathrm{S}}^{\mathrm{ee}}$ in equation (2.13) is

$$\nu_{\mathrm{S}}^{\mathrm{ee}} = \frac{1}{\tau_{\mathrm{c}}}\frac{\gamma^2}{\bar{p}^3}\frac{1}{\ln\Lambda_0}\left(\ln\Lambda^{\mathrm{ee}}\frac{\bar{p}^2}{\gamma^2}\Psi_{\mathrm{S}}(\bar{p},\Theta) + h(\bar{p})\right), \tag{2.27}$$

where we note that the first term approaches unity in the superthermal limit by equation (2.18) and if the energy dependence of the Coulomb logarithm is ignored. The second term is defined as

$$h(\bar{p}) = \sum_j \frac{n_j}{n_\mathrm{e}} N_{\mathrm{e},j} \left\{ \frac{1}{5} \ln \left[1 + \left(\frac{\bar{p}\sqrt{\gamma - 1}}{I_j / m_\mathrm{e} c^2} \right)^5 \right] - \beta^2 \right\}, \tag{2.28}$$

where I_j is the mean excitation energy. Values of I_j are tabulated by Sauer *et al.* (2015) for argon, neon and a few other fusion-relevant ions. Moreover, Berger *et al.* (1984) provide the values for a large number of elements, but only for neutral atoms. For other ion species, Mehlhorn (1981) suggested an interpolation formula which relates the mean excitation energy of an ion to that of a neutral atom, which gives satisfactory results at least for weakly ionized aluminium (Garbet & Deutsch, 1986).

Apart from their effect on the small-angle Fokker–Planck operator, partially ionized impurities also affect the avalanche operator, which describes large-angle collisions. Since the energy transfer required to produce a runaway electron typically far exceeds the binding energy, the analytic structure of the avalanche source is largely unaffected by collisions with partially ionized impurities. The only difference is that the multiplying density should include the free as well as the bound electrons, since they have equal probability of becoming runaway electrons. The effect of screening on the avalanche growth rate is discussed in section 3.3.2.

2.4 Kinetic equation for runaway electrons

In the previous sections, we discussed the specialization of the collision operator to make it suitable for runaway modeling, namely a relativistic collision operator, a large-angle collision operator and the modification due to screening in partially ionized plasmas. Apart from these effects, kinetic modeling of runaway electrons also requires the force in equation (2.1) to include radiation losses. Synchrotron radiation is emitted as particles gyrate around magnetic field lines, and bremsstrahlung emission is a result of inelastic collisions with ions (not to be confused with inelastic collisions with bound electrons in a partially ionized

plasma). Synchrotron radiation reaction can be modeled as a continuous momentum-dependent force (Decker *et al.*, 2016; Hirvijoki *et al.*, 2015*a*,*b*; Stahl *et al.*, 2015), whereas bremsstrahlung is dominated by large-angle collisions and generally requires a Boltzmann operator in order to capture the effect on the runaway distribution (Embréus *et al.*, 2016).

With the considerations above, we obtain an equation which describes the essential momentum-space effects of runaway dynamics. We introduce the cosine of the pitch angle $\xi = \cos\theta = \mathbf{p}\cdot\mathbf{B}/(pB)$ and let E be the component of the electric field antiparallel to the magnetic field $\mathbf{B}$ (so that electrons are accelerated in the positive ξ direction).[4] After a transformation to the $\{p, \xi\}$ coordinate system, we arrive at the kinetic equation in a homogeneous plasma:

$$\frac{\partial f_\mathrm{e}}{\partial t} + \underbrace{eE\left(\xi\frac{\partial f_\mathrm{e}}{\partial p} + \frac{1-\xi^2}{p}\frac{\partial f_\mathrm{e}}{\partial \xi}\right)}_{\text{electric field}} = \underbrace{C_\mathrm{FP} + C_\mathrm{ava}}_{\text{collisions}} + \underbrace{C_\mathrm{br} - \nabla_k\left(F^k_\mathrm{syn} f_\mathrm{e}\right)}_{\text{radiation reaction}}. \tag{2.29}$$

Here, the test-particle part of the linear Fokker–Planck collision operator C_FP was given in equation (2.12), the avalanche process is described by C_ava, and radiation losses are modeled by C_br (the bremsstrahlung collision operator) and $\mathbf{F}_\mathrm{syn}$ (the synchrotron radiation reaction force). Additionally, equation (2.29) can be supplemented by terms describing sources of energy and momentum to the system (such as terms to account for the spatial dynamics).

2.5 Numerical solution of the kinetic equation with CODE

While certain aspects of runaway dynamics can be understood directly from analytic equations, quantitative results typically rely on numerical calculations. This thesis is no exception: in Papers A-E the numerical tool CODE (COllisional Distribution of Electrons) (Landreman *et al.*,

[4] In a tokamak, particles are accelerated in the direction parallel (or antiparallel) to the *magnetic* field, since the motion caused by the orthogonal electric field will cancel by design of the tokamak. In a non-magnetized atmospheric plasma, ξ is instead defined by the angle to the electric field; $\xi = -\mathbf{p}\cdot\mathbf{E}/(pE)$.

2014; Stahl *et al.*, 2016) has an important role. CODE solves the kinetic equation in a uniform plasma as given in equation (2.29). It calculates the time-evolving electron distribution function f_e under the influence of electric-field acceleration, collisions and radiation reaction. It can also handle a prescribed evolution of background temperature and plasma composition, which is modeled by adding particle and heat sources to the kinetic equation (2.29). As a result of using a linearized collision operator, CODE can only handle a trace runaway population which may, however, give a non-trace contribution to the plasma current. Since modeling of non-trace runaway currents requires a self-consistent electric field evolution, the electric field in CODE can either be set externally or determined self-consistently by a zero-dimensional induction model.

CODE is equipped with linear operators for both small-angle (Fokker–Planck) and large-angle (Boltzmann) collisions. The Fokker–Planck operator includes the test-particle collision operator given in equation (2.10) as well as a non-relativistic field-particle operator (Landreman *et al.*, 2014). The possibility to model collisions with partially ionized impurities was added to the Fokker–Planck test-particle operator in conjunction with Paper A. CODE also contains several options for the avalanche operator. In its most advanced form, the implemented avalanche operator is fully conservative, which means that the runaway-generating field-particle term (see section 2.2.1) is combined with a test-particle term, which describes how the runaway-electrons are scattered by large-angle collisions (Embréus *et al.*, 2018). In accordance with the discussion in the previous section, a Boltzmann operator is also employed for bremsstrahlung radiation reaction, while synchrotron radiation reaction is modeled as a continuous force.

As for its numerical implementation, CODE is a continuum code. Since the pitch-angle dependence of the linearized Fokker-Planck and Boltzmann collision operators is diagonal in a Legendre polynomial basis (Helander & Sigmar, 2005), the kinetic equation is discretized in N_ξ Legendre modes P_L, so that

$$f_\mathrm{e}(p,\xi) = \sum_{L=0}^{N_\xi-1} f_L(p) P_L(\xi). \tag{2.30}$$

This is combined with a fourth-order finite difference scheme in the p variable, with N_p non-uniformly spaced grid points. The kinetic equation is thus represented on a $N_pN_\xi \times N_pN_\xi$ grid. The discretized Fokker–

Planck collision operator, the electric field terms and synchrotron radiation together form a sparse matrix and are treated implicitly in time, but the Boltzmann integral operators for avalanche and bremsstrahlung radiation reaction constitute dense matrices and are consequently treated explicitly for computational efficiency.

The computational power needed for a CODE simulation heavily depends on the problem: simple scenarios can run in a fraction of a second on a laptop, whereas a self-consistent electric-field simulation with an advanced avalanche operator including both bremsstrahlung and synchrotron radiation losses may require hundreds of CPU hours using more than 100 GB of RAM. The present thesis contains the results of both light and computationally demanding CODE calculations. The results of these simulations will be summarized in the final chapter, but first we will present some basic insights into runaway-electron dynamics that can be obtained from an analytical approach.

Chapter 3

Runaway-electron formation and decay

Having presented the essential components of a kinetic equation for runaway electrons in (2.29) in the previous chapter, we now interrogate this equation to gain some physical insights. Starting by deriving the fundamental equation for the runaway phenomenon, we subsequently identify the key parameter regimes in terms of time scales, electric field strength and plasma current. We also discuss the three chronological phases of runaway generation in tokamaks: seed generation, avalanche multiplication and runaway decay.

3.1 The runaway phenomenon

The runaway mechanism originates in the non-monotonic property of the dynamical friction force, which is defined as $p\nu_{\mathrm{S}}^{\mathrm{ee}}$ introduced in section 2.2.1. At superthermal speeds, the dynamical friction is identical to the mean force acting on a test particle. This can be seen from the electron momentum equation for a test particle homogeneously distributed in space but localized in momentum according to

$$f_{\mathrm{e}} = \delta^3(\mathbf{p} - \mathbf{p_0}) = \frac{1}{p^2 \sin\theta}\delta(p - p_0)\delta(\theta - \theta_0)\delta(\phi - \phi_0). \tag{3.1}$$

By taking the first p moment of the Fokker-Planck equation (2.1) with f_{e} as above, and using the test-particle collision operator from equa-

tion (2.12), we obtain the following in the absence of other forces acting on the particle:

$$\frac{\partial p_0}{\partial t} = \int p \left(\nu_{\mathrm{D}}^{\mathrm{ee}} + \nu_{\mathrm{D}}^{\mathrm{ei}}\right) \mathscr{L}\{f_{\mathrm{e}}\} d^3p + \int p \frac{1}{p^2} \frac{\partial}{\partial p} \left[p^3 \left(\nu_{\mathrm{S}}^{\mathrm{ee}} f_{\mathrm{e}} + \frac{1}{2} \nu_{\parallel}^{\mathrm{ee}} p \frac{\partial f_{\mathrm{e}}}{\partial p}\right)\right] d^3p. \tag{3.2}$$

The first term evaluates to zero when integrating over θ and ϕ, respectively:

$$\int \frac{p^3}{2} \left(\nu_{\mathrm{D}}^{\mathrm{ee}} + \nu_{\mathrm{D}}^{\mathrm{ei}}\right) \left[\frac{\partial}{\partial \theta} \left(\sin\theta \frac{\partial f_{\mathrm{e}}}{\partial \theta}\right) + \frac{1}{\sin\theta} \frac{\partial^2 f_{\mathrm{e}}}{\partial \phi^2}\right] dp\, d\theta\, d\phi = 0. \tag{3.3}$$

Moreover, $\nu_{\parallel}^{\mathrm{ee}}$, defined in equation (2.13), vanishes at superthermal momentum. Upon evaluating the angular integrals, equation (3.2) therefore yields

$$\frac{\partial p_0}{\partial t} = \int_0^\infty p \frac{\partial}{\partial p} \left(p^3 \nu_{\mathrm{S}}^{\mathrm{ee}} \frac{\delta(p - p_0)}{p^2}\right) dp = -p_0 \nu_{\mathrm{S}}^{\mathrm{ee}}(p_0), \tag{3.4}$$

integrating by parts in the last step.

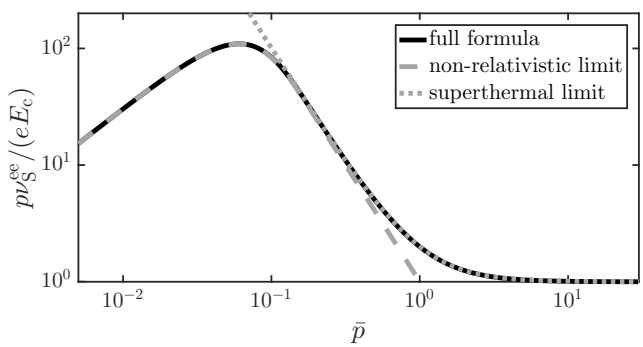

Figure 3.1: Dynamical friction force on an electron in a fully ionized plasma of temperature 1 keV (i.e. $\Theta \approx 2 \cdot 10^{-3}$; $\bar{p}_{\mathrm{Te}} \approx 0.06$), neglecting the energy-dependence of the Coulomb logarithm. The solid black line uses the full expression (2.13), whereas the gray lines show the limiting expressions (3.5). Note that radiation reaction also contribute to the energy loss at high energies, which means that the total friction on a relativistic electron increases with $\bar{p}$.

Using equations (2.21) and (2.22) obtained in a fully ionized plasma and for non-relativistic bulk temperatures $\Theta = T_\mathrm{e}/m_\mathrm{e}c^2 \ll 1$, the dynamical friction force is given by

$$F = p\nu_\mathrm{S}^\mathrm{ee} \rightarrow \begin{cases} \dfrac{m_\mathrm{e}c}{\tau_\mathrm{c}} \dfrac{\ln\Lambda^\mathrm{ee}}{\ln\Lambda_0} \dfrac{G(x)}{\Theta}, & \bar{p} \ll 1, \\ \dfrac{m_\mathrm{e}c}{\tau_\mathrm{c}} \dfrac{\ln\Lambda^\mathrm{ee}}{\ln\Lambda_0} \dfrac{\gamma^2}{\bar{p}^2}, & \gamma - 1 \gg \Theta. \end{cases} \tag{3.5}$$

The friction force is plotted in figure 3.1, comparing the full expression using equation (2.13) with the limiting expressions in equation (3.5). The friction force increases for subthermal velocities, and then decreases with momentum above the thermal velocity, approaching a constant value in the high-energy limit. This behavior is thus characterized by two important scales for the electric field: the *critical electric field* E_c and the *Dreicer field* E_D.

The critical electric field is the threshold electric field above which the runaway process can occur. This field can be identified by taking the high-energy limit of the superthermal expression in equation (3.5), neglecting the energy-dependence of $\ln\Lambda$. Then, eE_c is the force required to balance the collisional friction on a high-energy particle moving parallel to the electric field:

$$E_\mathrm{c} = \frac{m_\mathrm{e}c}{e\tau_\mathrm{c}} = \frac{n_\mathrm{e}e^3 \ln\Lambda_0}{4\pi\epsilon_0^2 m_\mathrm{e}c^2}, \tag{3.6}$$

where the relativistic collision time τ_c was given in equation (2.14).

For $E > E_\mathrm{c}$, sufficiently energetic particles will be continuously accelerated, and can accordingly be labeled as runaway electrons. To be more precise, we can define the critical momentum above which electric-field acceleration overcomes collisional friction if the electron travels parallel to the electric field. Combining the superthermal limit of the friction force (3.5) with equation (3.6), and once again neglecting the energy-dependence of the Coulomb logarithm, $\bar{p}_\mathrm{c}$ is obtained from

$$eE = eE_\mathrm{c}\frac{\bar{p}_\mathrm{c}^2 + 1}{\bar{p}_\mathrm{c}^2} \Rightarrow \bar{p}_\mathrm{c} = \frac{1}{\sqrt{E/E_\mathrm{c} - 1}}. \tag{3.7}$$

The concept of a threshold field for runaway generation can be generalized beyond the force balance calculation above. The *effective critical*

electric field $E_{\mathrm{c}}^{\mathrm{eff}}$ can be defined as the minimum electric field required to sustain a relativistic runaway distribution indefinitely, and is higher than E_{c} for several reasons. Electrons moving with an angle θ to the electric field experience a force $\mathbf{F}_{\mathrm{E}} \cdot \hat{\mathbf{p}} = -eE\cos\theta$ projected in the $\hat{\mathbf{p}} = \mathbf{p}/p$ direction, and thus the electric field may need to significantly exceed E_{c} in order to balance out the widening of the distribution function caused by pitch-angle scattering. Moreover, the slowing-down force is increased at relativistic electron speeds due to the effect of bremsstrahlung and synchrotron radiation reaction as well as an energy-dependent Coulomb logarithm, and partial screening contributes to enhanced collision rates in partially ionized plasmas. The enhancement of the critical electric field due to these three effects is the subject of Paper C, where we determined the value of $E_{\mathrm{c}}^{\mathrm{eff}}$ in a plasma dominated by partially ionized impurities. In Paper C, we employed a method developed by Lehtinen *et al.* (1999) and Aleynikov & Breizman (2015), which assumes fast pitch-angle dynamics, and showed that in the presence of partially ionized impurities, the effective critical field is approximately given by

$$E_{\mathrm{c}}^{\mathrm{eff}} \gtrsim E_{\mathrm{c}}^{\mathrm{tot}} = \frac{n_{\mathrm{e}}^{\mathrm{tot}}}{n_{\mathrm{e}}} E_{\mathrm{c}}, \tag{3.8}$$

where $n_{\mathrm{e}}^{\mathrm{tot}}$ is the total electron density including free and bound electrons. Consequently, bound and free electrons contribute approximately equally to the critical electric field. This result is the combined effect of collisional friction and enhanced pitch-angle scattering, in synergy with radiation reaction losses.

While the critical electric field sets the scale for the runaway mechanism to occur at all, the Dreicer field determines if the electric field is sufficient to accelerate a substantial runaway tail starting from a Maxwellian distribution. Accordingly, the Dreicer field is related to the fraction of the thermal population that experiences a net electric-field acceleration; E_{D} approximates the required electric field for *slide-away*, i.e. when the entire electron distribution is accelerated (Dreicer, 1959). To estimate the slide-away electric field, consider the maximum of the dynamical friction force in the non-relativistic limit of equation (3.5)

$$\max[F] = eE_{\mathrm{c}} \frac{m_{\mathrm{e}}c^2}{T_{\mathrm{e}}} \max[G(x)] \approx 0.2eE_{\mathrm{D}}, \tag{3.9}$$

where the Dreicer field evaluates to

$$E_{\mathrm{D}} = E_{\mathrm{c}} \frac{m_{\mathrm{e}}c^2}{T_{\mathrm{e}}}. \tag{3.10}$$

If the electric field is close to this slide-away field, the entire electron distribution will be distorted and rapidly deviate from a Maxwellian. In contrast, if the electric field is a few percent of E_D, it will only accelerate the small fraction of particles that are sufficiently fast to experience a positive net force. Due to energy diffusion (described by $\nu_\parallel$ introduced in section 2.2.1), this region in momentum space will be continuously re-populated, which gives the distribution an energetic tail of runaway electrons (Helander *et al.*, 2002). This runaway population will constitute a small, steadily growing fraction of the electron population, while the majority of the distribution will remain close to the Maxwellian distribution. This mechanism of runaway production is known as Dreicer generation.

To summarize, there are three distinct electric-field regions with different fast-electron behavior:

(i) $E < E_\mathrm{c}^\mathrm{eff}$: runaway decay,

(ii) $E_\mathrm{c}^\mathrm{eff} < E \lesssim 0.2E_\mathrm{D}$: runaway generation can occur,

(iii) $E \gtrsim 0.2E_\mathrm{D}$: slide-away.

Of these, the electric field is typically in range (ii) during runaway scenarios, and consequently this is the most important region to model from a runaway perspective. In this range [as well as range (i)], a linear collision operator is adequate as long as the runaway population is trace.

In tokamak experiments, runaway generation is usually characterized by three phases: seed generation, avalanche multiplication and decay. These phases are further discussed in section 3.3, but first a brief interlude on the induced electric field, which separates the runaway-generation phases.

3.2 Induced electric field in tokamak disruptions

The basic equations for the electric field induced in a tokamak disruption can be directly obtained from Maxwell's equations. Neglecting the

displacement current in Ampère's law, these are

$$\mathbf{B} = \nabla \times \mathbf{A}, \tag{3.11}$$

$$\mathbf{E} = -\nabla\Phi - \frac{\partial \mathbf{A}}{\partial t}, \tag{3.12}$$

$$\nabla \times \mathbf{B} = \mu_0 \mathbf{j}, \tag{3.13}$$

$$\nabla \times \mathbf{E} = -\frac{\partial \mathbf{B}}{\partial t}. \tag{3.14}$$

From Maxwell's equations, we can derive a few basic relations governing the induced electric field during and after tokamak disruptions: the time integral of the electric field, its time evolution when the runaway current is small and the maximum electric field after the thermal quench.

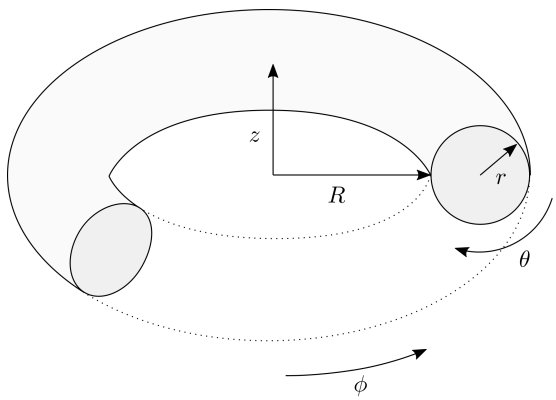

Figure 3.2: A torus showing common tokamak coordinates, including the poloidal and toroidal angles, which are denoted θ and φ, respectively. The radial coordinate r may alternatively be parametrized with the poloidal flux ψ_p (or the toroidal flux ψ_t).

3.2.1 Relation between induced electric field and the poloidal flux

Figure 3.2 shows the tokamak geometry, including the *poloidal* and *toroidal* angles. To confine the plasma particles, the magnetic field forms a helical pattern, with a large toroidal component and a smaller poloidal component induced by a toroidal current. Both the toroidal magnetic

field and current can have either sign depending on the tokamak configuration, which means that the induced electric field can be either toroidal or anti-toroidal. For simplicity, we will here assume that both $B_\varphi > 0$ and $j_\varphi > 0$, so that $B_\theta > 0$ and $E_\varphi > 0$.

A key parameter describing the magnetic field geometry is the *poloidal flux* ψ_p, which is the flux of magnetic field through the central hole of the torus (Boozer, 2005):

$$\psi_\mathrm{p} = -\int \mathbf{B} \cdot d\mathbf{a}_\theta, \tag{3.15}$$

where $d\mathbf{a}_\theta$ is the area element perpendicular to $\nabla\theta$. Surfaces of constant ψ_p (which, for example, could be the surface of the torus in figure 3.2), together form the nested torii known as flux surfaces, and describe the magnetic field structure in the tokamak. Accordingly, the poloidal flux can be regarded as a label for flux surfaces of the tokamak, and ψ_p is often used as a radial coordinate instead of r since it simplifies the expressions for e.g. the equilibrium magnetic field.

Using Stokes' theorem and the vector potential defined in equation (3.11), the poloidal flux can be rewritten

$$\psi_\mathrm{p} = -\int \mathbf{A} \cdot d\mathbf{l} = -2\pi R A_\varphi, \tag{3.16}$$

where the last equality comes from toroidal symmetry. Furthermore, again due to axisymmetry,

$$E_\varphi = -\frac{\partial A_\varphi}{\partial t} = \frac{1}{2\pi R}\frac{\partial \psi_\mathrm{p}}{\partial t}, \tag{3.17}$$

which implies that the change in poloidal flux during a tokamak disruption directly determines the time integral of the induced electric field:

$$\int E_\varphi \, dt = \frac{\Delta\psi_\mathrm{p}}{2\pi R}. \tag{3.18}$$

From the definition (3.15), $\psi_p < 0$ if $B_\theta > 0$, which implies that the poloidal flux will increase toward zero during a disruption, and the toroidal electric field will be positive with our assumed tokamak configuration. Since the electric field is integral to runaway dynamics, it may not be surprising that the change in poloidal flux is a fundamental quantity in runaway dynamics, which will be shown in section 3.3.2.

3.2.2 Induction equation in the cylindrical limit

Another equation that will be useful later on is the induction equation, which can be obtained by combining Ampère's and Faraday's laws:

$$\mu_0 \frac{\partial \mathbf{j}}{\partial t} = -\nabla \times (\nabla \times \mathbf{E}) = \nabla^2 \mathbf{E}, \tag{3.19}$$

since $\nabla \cdot \mathbf{E} = 0$ in a quasi-neutral plasma. An approximate form of the induction equation can be obtained in a cylindrically symmetric plasma, corresponding to a large-aspect-ratio tokamak. Since, by design of the tokamak, an electric field perpendicular to the magnetic field causes no net acceleration, we project equation (3.19) in the direction parallel to the magnetic field. As the magnetic field lines are approximately toroidal, we get the following in the cylindrical approximation $E_\parallel \approx E_\varphi(r)$:

$$\mu_0 \frac{\partial j_\parallel}{\partial t} = \nabla^2 E_\parallel = \frac{1}{r}\frac{\partial}{\partial r}\left(r \frac{\partial E_\parallel}{\partial r}\right). \tag{3.20}$$

In elongated plasmas, where the cross-section of the torus is elliptical rather than circular, the induction equation acquires a dependence on the elongation κ, as shown in Paper I. The direct effect of finite κ is a modest increase in the induced electric field at fixed current decay rate, but this effect is overwhelmed by the reduction in $j_\parallel$ if the minor radius a and the current $I_\parallel \sim \kappa a^2 j_\parallel$ are kept constant while varying κ.

In the cylindrical limit, we can obtain an explicit expression for the poloidal flux by combining equations (3.17) and (3.20):

$$\psi_\mathrm{p}(r) = -\mu_0 R \int_r^a \frac{I(r')}{r'} dr' + \psi_\mathrm{p}(a), \tag{3.21}$$

where $I(r') \equiv 2\pi \int_0^{r'} j_\parallel(r) r dr$. If there is a perfectly conducting wall at $r = a$, $\psi_\mathrm{p}(a)$ must be constant in time not to induce an electric field in the wall, which implies that only the first term in equation (3.21) contributes to induce an electric field.

The electric field evolution is also related to the current density through Ohm's law. In a non-relativistic plasma with a weak electric field (Helander & Sigmar, 2005),

$$\begin{aligned} j_{\parallel,\Omega} &= \sigma_\parallel E_\parallel, \\ \sigma_\parallel &= \frac{n_\mathrm{e} e^2 \tau_\mathrm{ei}}{m_\mathrm{e}} L_{11} = \frac{12\pi^{3/2}}{\sqrt{2}} \frac{T_\mathrm{e}^{3/2} \epsilon_0^2}{Z_\mathrm{eff}\, e^2 \sqrt{m_\mathrm{e}} \ln \Lambda_0} L_{11}, \end{aligned} \tag{3.22}$$

where τ_{ei} is the thermal electron-ion collision time and L_{11} varies slowly with increasing effective charge from approximately 2.0 at $Z_{\mathrm{eff}} = 1$ to 3.4 as $Z_{\mathrm{eff}} \to \infty$. There are further corrections to the conductivity, for example at relativistic plasma temperatures (Braams & Karney, 1989), but the general scaling with physical parameters persists when these corrections are included. In equation (3.22), $j_{\parallel,\Omega}$ is the Ohmic current and signifies that the equation only applies to the thermal plasma population. The current produced by runaway electrons is not determined by Ohm's law since it breaks the weak-electric-field ordering, is sensitive to transient behavior (whereas equation (3.22) is derived in steady state) and also can be generated through large-angle collisions. Accordingly, the parallel current is given by $j_\parallel = \sigma_\parallel E_\parallel + j_{\mathrm{RE}}$, which can be used as a definition of the runaway current density j_{RE}.

The induction equation (3.20) and Ohm's law (3.22) can be combined to approximate the evolution of the electric field and the current in the phase where the contribution from runaway electrons can be neglected. This is useful both to estimate the current quench time and to get an upper estimate of the induced electric field during the current quench – the latter was used in Paper D to study avalanche dynamics. In the limit of trace runaway current, the electric field evolution can be determined by separation of variables. Assuming

$$j_\parallel(r,t) = \sum_n c_n j_n(r) \mathrm{e}^{-t/\tau_n^{\mathrm{CQ}}}, \tag{3.23}$$

equation (3.20) can be written

$$\bar{r}^2 j_n''(\bar{r}) + \bar{r} j_n'(\bar{r}) = -\frac{\mu_0 \sigma_\parallel a^2}{\tau_n^{\mathrm{CQ}}} \bar{r}^2 j_n, \tag{3.24}$$

where $\bar{r} = r/a \in [0,1]$ is the radial coordinate normalized to the minor radius of the tokamak. This equation is solved by J_0, the zeroth-order Bessel function of the first kind. If a conducting wall is assumed at the plasma edge $\bar{r} = 1$, the boundary condition is $j_n(1) = 0$, from which we obtain

$$\begin{cases} j_n = J_0\left(x_n \bar{r}\right), \\ \tau_n^{\mathrm{CQ}} = \dfrac{\mu_0 \sigma_\parallel a^2}{x_n^2}, \end{cases} \tag{3.25}$$

where x_n is the n'th zero of $J_0(x)$; for example, $x_1 \approx 2.4$.

Assuming that the initial current profile is described by the first Bessel mode corresponding to $n = 1$, we obtain

$$\begin{cases} j_\parallel(\bar{r}, t) = \dfrac{x_1}{2J_1(x_1)} \dfrac{I_0}{\pi a^2} J_0(x_1 \bar{r}) \mathrm{e}^{-t/\tau_{\mathrm{CQ}}}, \\ \tau_{\mathrm{CQ}} = \dfrac{\mu_0 \sigma_\parallel a^2}{x_1^2}, \end{cases} \tag{3.26}$$

where the current density was normalized to give an initial plasma current $I_0 = 2\pi \int_0^a r j_\parallel(\bar{r}, 0) dr$. We can then estimate the current quench time

$$\tau_{\mathrm{CQ}} = 13\,\mathrm{ms} \times \frac{(T_\mathrm{e}\,[10\,\mathrm{eV}])^{3/2} (a\,[\mathrm{m}])^2}{Z_\mathrm{eff}}, \tag{3.27}$$

where we approximated $L_{11} \approx 2$, and $\ln\Lambda \approx 10$ represents a typical post-disruption value. During normal plasma operation, where the temperature is in the keV range, the current decay would take many seconds (if the current drive was turned off). Therefore, the current quench mainly takes place after the thermal quench, which typically occurs on the sub-ms timescale in medium-sized tokamaks (such as ASDEX Upgrade and DIII-D, which both have $a \approx 0.5\,\mathrm{m}$), and is expected to last several ms in ITER (where $a \approx 2\,\mathrm{m}$) (Hender *et al.*, 2007). This also indicates that the thermal quench and the current quench can be treated as separate events, unless the post-disruption temperature is lower than approximately 5 eV.

If the thermal and current quench can be separated in time (i.e. $\tau_{\mathrm{TQ}} \ll \tau_{\mathrm{CQ}}$), the maximum induced electric field can be estimated from Ohm's law (3.22) and demanding that the current density does not change during the thermal quench[1]:

$$\sigma_{\text{post-TQ}} E_{\text{post-TQ}} \approx j_{\parallel,\text{initial}}. \tag{3.28}$$

[1] One exception where the constant-current assumption is violated is during the violent onset of the disruption, where MHD effects cause magnetic surfaces to break and reconnect. In this case, magnetic helicity conservation tends to flatten out the current profile and cause a sudden peak in the plasma current (Boozer, 2019). The initial current density $j_{\parallel,\text{initial}}$ should then be evaluated after the magnetic reconnection.

With the current profile from equation (3.26), the central ($r = 0$) induced electric field is

$$\frac{E_{\text{post-TQ}}}{E_{\text{c}}} \approx \frac{j_{\parallel,\text{initial}}}{n_{\text{e}} e c} \frac{\sqrt{2}}{3\sqrt{\pi}} \frac{Z_{\text{eff}}}{L_{11}} \left(\frac{m_{\text{e}} c^2}{T} \right)^{3/2} \approx 200 \, \frac{I_0 \, [\text{MA}] \, Z_{\text{eff}}}{n_{\text{e}} \, [10^{20} \, \text{m}^{-3}] (T \, [10 \, \text{eV}])^{3/2} (a \, [\text{m}])^2} \,, \tag{3.29}$$

where all quantities should be evaluated after the thermal quench, and we used equations (3.6) and (3.22). In large tokamaks, we may therefore expect post-disruption electric fields of hundreds to a thousand times the critical electric fields.

Also $E/E_{\text{D}} = (T_{\text{e}}/m_{\text{e}}c^2)E/E_{\text{c}}$ (by equation (3.10)) is expected to peak at the end of the thermal quench, although the weaker temperature dependence can here be canceled by a substantial increase in the plasma density during the disruption;

$$\frac{E_{\text{post-TQ}}}{E_{\text{D}}} \approx 0.5 \, \% \times \frac{I_0 \, [\text{MA}] \, Z_{\text{eff}}}{n_{\text{e}} \, [10^{20} \, \text{m}^{-3}] (T_{\text{e}} \, [10 \, \text{eV}])^{1/2} (a \, [\text{m}])^2} \,. \tag{3.30}$$

3.2.3 Zero-dimensional equation for the induced electric field

Finally, the simplest equation for the induced electric field is the zero-dimensional induction equation. For this purpose, we introduce the flux inductance (Boozer, 2018)

$$L = \left| \frac{\Psi_{\text{p}}}{I_{\text{p}}} \right| , \tag{3.31}$$

where $\Psi_{\text{p}} = \psi_{\text{p}}(r = 0)$ and $I_{\text{p}} = I(r = a)$ is the total plasma current. The flux inductance generally differs from the self-inductance of the plasma (Boozer, 2018), but the two quantities are equivalent in the limit where the plasma becomes a thin conducting wire (Bellan, 2004, chapter 9.6).

Using the flux inductance, the induced electric field can be related to the current evolution through equation (3.17),

$$E_{\parallel}(r = 0) = -\frac{1}{2\pi R} \frac{\partial L I_{\text{p}}}{\partial t} \approx -\frac{L}{2\pi R} \frac{\partial I_{\text{p}}}{\partial t} , \tag{3.32}$$

if the inductance varies slowly in time. This zero-dimensional inductance equation can be used for a simplified analysis of the current dynamics, as was done for example in Paper C and by Helander *et al.* (2002).

3.3 Dynamics during runaway generation and decay

As stated at the end of section 3.1, runaway dynamics can be divided into three chronological phases, especially in large tokamaks. First, an initial seed population is generated through, for example, the Dreicer mechanism. This seed is then amplified by the avalanche mechanism until the Ohmic plasma current is consumed. Finally, this runaway population decays.

3.3.1 Runaway seed generation

Runaway seed generation can occur through several processes. *Hot-tail* generation takes place if the electron distribution cools down while it is subject to an electric field (Aleynikov & Breizman, 2017; Chiu *et al.*, 1998; Helander *et al.*, 2004; Smith & Verwichte, 2008; Smith *et al.*, 2005). Since the superthermal friction force decreases with speed, the highly energetic tail of the distribution will be cooled at a slower rate than the thermal population, if the cooling is dominated by collisional processes. When this bulk cooling is accompanied by an electric field, as in a disruption, the hot-tail mechanism can produce a runaway seed population or even convert a large part of the initial current directly (Aleynikov & Breizman, 2017).

During the active phase of fusion operation, fast electrons can be generated through tritium decay and Compton scattering of γ-rays emitted from the activated wall. Provided that the electric field is sufficiently large, a fraction of the produced fast electrons will exceed the critical momentum and thus run away. For tritium decay, the maximum electron energy is 18.6 keV, which implies a threshold $E \gtrsim 15E_\mathrm{c}$ for runaway production through tritium decay, but the runaway generation drops significantly already below $E \approx 50E_\mathrm{c}$ (Martín-Solís *et al.*, 2017). The tritium seed is indirectly affected by partial screening, since the increased critical momentum reduces the fraction of produced electrons above the runaway threshold (Paper K).

Based on estimations for the ITER wall, runaway production through Compton decay is less sensitive to the critical momentum and thus the electric field; it is reduced below $E \gtrsim 10E_\mathrm{c}$ but occurs down to $E \approx E_\mathrm{c}$ (Martín-Solís *et al.*, 2017). Moreover, Compton-scattered electrons can have such a high energy that they may survive even if they

are generated before the thermal quench, similarly to the hot-tail mechanism.

Runaway seed generation can also occur through the *Dreicer mechanism*, which is the combined effect of electric-field acceleration and collisional diffusion (Dreicer, 1959, 1960). The most accurate analytical expression for the Dreicer generation rate was obtained by Connor & Hastie (1975) by generalizing the non-relativistic results by Kruskal & Bernstein (1962),

$$\frac{dn_{\mathrm{RE}}}{dt} = C\frac{n_{\mathrm{e}}}{\tau_{\mathrm{ee}}}\left(\frac{E}{E_{\mathrm{D}}}\right)^{-\frac{3}{16}(1+Z_{\mathrm{eff}})h} \exp\left(-\lambda\frac{E_{\mathrm{D}}}{4E} - \sqrt{\eta\frac{(1+Z_{\mathrm{eff}})E_{\mathrm{D}}}{E}}\right), \tag{3.33}$$

$$\lambda = 8\frac{E^2}{E_{\mathrm{c}}^2}\left(1 - \frac{1}{2}\frac{E_{\mathrm{c}}}{E} - \sqrt{1-\frac{E_{\mathrm{c}}}{E}}\right),$$

$$\eta = \frac{1}{4}\frac{E^2}{E_{\mathrm{c}}(E-E_{\mathrm{c}})}\left[\frac{\pi}{2} - \arcsin\left(1 - \frac{2E_{\mathrm{c}}}{E}\right)\right]^2,$$

$$h = \frac{1}{3}\frac{1}{\frac{E}{E_{\mathrm{c}}}-1}\left[\frac{E}{E_{\mathrm{c}}} + 2\left(\frac{E}{E_c} - 2\right)\sqrt{\frac{E}{E-E_{\mathrm{c}}}} - \frac{Z_{\mathrm{eff}}-7}{Z_{\mathrm{eff}}+1}\right].$$

Here,

$$\tau_{\mathrm{ee}} = \frac{4\pi\varepsilon_0^2 m_{\mathrm{e}}^2 v_{\mathrm{Te}}^3}{n_{\mathrm{e}} e^4 \ln\Lambda_0} \tag{3.34}$$

is the thermal electron collision time, with the thermal speed $v_{\mathrm{Te}} = \sqrt{2T_{\mathrm{e}}/m_{\mathrm{e}}}$. The order-unity parameter C is undetermined by Connor & Hastie (1975) but has been quantified in subsequent work to around $C \approx 1.0$ if the thermal collision time is defined as above (Jayakumar *et al.*, 1993; Kruskal & Bernstein, 1962). The parameters λ, η and h constitute the relativistic generalization of the generation rate; they approach unity as $E/E_{\mathrm{c}} \to \infty$.

As the Dreicer generation rate is exponentially sensitive to E/E_{D}, Dreicer generation predominantly occurs when the electric field is largest. As shown in equation (3.30), this is most likely immediately after the thermal quench. Despite its apparent complexity, equation (3.33) is only valid for fully ionized plasmas. In partially ionized plasmas, the generation rate can decrease by several orders of magnitude, which we showed in Paper E. In this paper, we performed a large number of CODE simulations to determine the Dreicer generation rate in plasmas of various

ionization degree, and used this data to train a neural network. The neural network is parametrized by a series of matrix multiplications and function applications:

$$\ln\left(\frac{\tau_{\mathrm{ee}}}{n_{\mathrm{e}}}\frac{dn_{\mathrm{RE}}}{dt}\right) = \mathbf{W}_5 \tanh\left[\mathbf{W}_4 \cdots \tanh(\mathbf{W}_1\mathbf{x} + \mathbf{b}_1) + \cdots + \mathbf{b}_4\right] + \mathbf{b}_5. \tag{3.35}$$

Here, $\mathbf{x}$ is an eight-component input vector composed of E/E_{D}, $\ln T_{\mathrm{e}}$ and six parameters related to the plasma composition. To determine the weight matrices $\mathbf{W}_{(k)}$ and the bias vectors $\mathbf{b}_{(k)}$, the neural network was trained using the Python library PyTorch (Paszke *et al.*, 2019).

As noted above, runaway seed generation mostly takes place during the thermal quench and the early phase of the current quench. This phase, in particular the thermal quench and the associated breakup of magnetic flux surfaces, is characterized by uncertainties in physical models. Most notably, a large fraction of the runaway seed may be lost due to transport, something which has not been systematically analyzed apart from a few examples. If transport effects are neglected, it is estimated that hot-tail generation dominates in ITER, followed by tritium decay and Compton scattering. Dreicer generation is typically negligible in ITER compared to the other sources (Martín-Solís *et al.*, 2017), but it is believed to often dominate in today's medium-sized tokamaks, which have lower temperatures and do not produce fusion reactions, in particular for relatively long thermal quench times (Smith *et al.*, 2005).

3.3.2 Avalanche multiplication

Once a seed population of runaway electrons has been generated, it can grow exponentially through the avalanche mechanism, provided that the electric field is larger than the effective critical electric field (Jayakumar *et al.*, 1993; Sokolov, 1979). This avalanche is created when a runaway electron collides with a thermal electron and transfers enough momentum that both electrons run away. Large-angle collisions thereby provide a shortcut in momentum-space compared to the combination of collisional diffusion and electric field acceleration that gives Dreicer generation. As a result, if the runaway population is sufficiently large, this mechanism will dominate over Dreicer and hot-tail generation, despite the rarity of large-angle collisions in plasmas mentioned in the previous chapter. The small-angle Fokker–Planck operator must therefore

be complemented by the large-angle Boltzmann operator in order to accurately describe runaway generation.

In a fully ionized, homogeneous plasma, the avalanche growth rate is given by Rosenbluth & Putvinski (1997):

$$\Gamma \equiv \frac{1}{n_{\mathrm{RE}}}\frac{\partial n_{\mathrm{RE}}}{\partial t} = \frac{e}{m_{\mathrm{e}} c \ln\Lambda_{\mathrm{c}}}\frac{|E_{\parallel}| - E_{\mathrm{c}}}{\sqrt{5+Z_{\mathrm{eff}}}}. \tag{3.36}$$

Equation (3.36) was derived assuming that all incoming runaway electrons are traveling with the speed of light and parallel to the electric field. These simplifying assumptions have been relaxed by Chiu *et al.* (1998) and Embréus *et al.* (2018), who showed that the growth rate (3.36) remains accurate in most of the parameter regime.

Avalanche generation takes place during the current quench when the flux surfaces have healed. Together with the fact that it is less sensitive to plasma parameters, the avalanche dynamics is therefore expected to be less sensitive to uncertainties in models and experimental measurements. To determine if avalanche generation is important in a certain scenario, the *avalanche multiplication factor* N_{ava} is a key parameter. The avalanche multiplication factor determines the upper limit on how much a runaway seed can be multiplied, i.e. how small a runaway seed is required to prevent significant avalanche generation. This parameter can be estimated by assuming that the magnetic field is purely toroidal, $E_{\parallel} = E_{\varphi}$. Furthermore, if $E_{\parallel} \gg E_{\mathrm{c}}$ we can integrate equation (3.36) in time, and use equation (3.18) to obtain

$$\begin{aligned} N_{\mathrm{ava}} \equiv \ln\frac{n_{\mathrm{RE}}}{n_{\mathrm{seed}}} &\approx \frac{e}{m_{\mathrm{e}} c \ln\Lambda_{\mathrm{c}}}\frac{1}{\sqrt{5+Z_{\mathrm{eff}}}}\int_0^{\infty} E_{\varphi}\, dt \\ &= \frac{e}{m_{\mathrm{e}} c \ln\Lambda_{\mathrm{c}}}\frac{1}{\sqrt{5+Z_{\mathrm{eff}}}}\frac{\Delta\psi_{\mathrm{p}}}{2\pi R}. \end{aligned} \tag{3.37}$$

As an example, we use the current profile from equation (3.26) obtained in the cylindrical limit $R \gg a$. The induced electric field on the magnetic axis then obeys

$$\int_0^{\infty} E_{\parallel} dt = \frac{\tau_{\mathrm{CQ}}}{\sigma_{\parallel}}\frac{x_1 J_0(0)}{2J_1(x_1)}\frac{I_0}{\pi a^2} = \frac{\mu_0}{2\pi}\frac{J_0(0)}{x_1 J_1(x_1)} I_0. \tag{3.38}$$

The avalanche multiplication factor is thus given by

$$\ln\frac{n_{\mathrm{RE}}}{n_{\mathrm{seed}}} \approx \frac{1.6}{\ln\Lambda_{\mathrm{c}}\sqrt{5+Z_{\mathrm{eff}}}}\frac{I_0}{I_{\mathrm{A}}}, \tag{3.39}$$

where $I_\mathrm{A} = (4\pi m_\mathrm{e} c)/(\mu_0 e) \approx 17\,\mathrm{kA}$ is the Alfvén current. This expression is rather robust since the temperature and density dependence canceled, except for the weak variation in the Coulomb logarithm. In an ITER-like plasma with parameters $I_0 = 15\,\mathrm{MA}$, $n_\mathrm{e} = 10^{20}\,\mathrm{m}^{-3}$, $T = 10\,\mathrm{eV}$ and $Z_\mathrm{eff} = 1$, $N_\mathrm{ava} \approx 37$, implying that a seed could be amplified with a striking factor[2] of 10^{16}. Consequently, substantial runaway generation is much more difficult to prevent in ITER compared to today's medium size tokamaks with approximately a tenth of the plasma current.

In practice, the runaway population typically carries an appreciable fraction of the current toward the end of the current quench. In this case, the runaway beam is not amplified by the full factor $\mathrm{e}^{N_\mathrm{ava}}$, since only a fraction of the poloidal flux (or plasma current) is consumed by the avalanche mechanism through the electric field. Accordingly, $\Delta\psi_\mathrm{p} < |\psi_\mathrm{p}(t=0)|$. The fact that no appreciable electric field will be induced after the runaway current reaches $I_\mathrm{RE} \approx I_p$ can be approximately accounted for in equation (3.39) by replacing I_0 with the associated change in the plasma current ΔI_p.

The simple result in equation (3.37), which was derived in a fully ionized plasma, becomes considerably more complicated in a partially ionized plasma, as we showed in Paper D. The generalized expression for the avalanche growth rate takes the form

$$\Gamma = \frac{e}{m_\mathrm{e} c \ln\Lambda_\mathrm{c}} \frac{n_\mathrm{e}^\mathrm{tot}}{n_\mathrm{e}} \frac{|E_\parallel| - E_\mathrm{c}^\mathrm{eff}}{\sqrt{4 + \bar{\nu}_\mathrm{S}(p_\star)\bar{\nu}_\mathrm{D}(p_\star)}}, \tag{3.40}$$

where $\bar{\nu}_\mathrm{S} = \nu_\mathrm{S}^\mathrm{ee}/(\tau_\mathrm{c}^{-1}\gamma^2/\bar{p}^3)$ and $\bar{\nu}_\mathrm{D} = \nu_\mathrm{D}/[\tau_\mathrm{c}^{-1}\gamma/\bar{p}^3]$ are the collision frequencies normalized to the superthermal, idealized expressions given in equation (2.22), and the partially screened collision frequencies are defined in equations (2.25) and (2.27). The effective critical electric field $E_\mathrm{c}^\mathrm{eff}$ is discussed in section 3.1 and is calculated in Paper C. The relation $p_\star^2 = \sqrt{\bar{\nu}_\mathrm{S}(p_\star)\bar{\nu}_\mathrm{D}(p_\star)}/(E_\parallel/E_\mathrm{c})$ defines an effective critical momentum $p_\star$ for runaway, which has a non-trivial dependence on the electric field in partially ionized plasmas.

When evaluating equation (3.40) in a partially ionized plasma, the avalanche growth rate is no longer directly proportional to the electric field,

[2]This number is somewhat different from the number stated in the introduction due to different assumptions on for example the plasma current profile.

which implies that the change in poloidal flux is not sufficient to determine the avalanche multiplication factor. Instead, the avalanche dynamics are sensitive to the electric-field evolution during the current quench. The reason for this more complicated behavior is fundamentally the energy-dependent enhancement of the collision frequencies due to partial screening. This results in two competing effects: the increased total density of electrons in the plasma increases the growth rate, but runaway electrons also experience more collisional friction and pitch-angle scattering. We find that the former effect always dominates, so the avalanche growth rate increases in the presence of partially ionized impurities, as opposed to the Dreicer generation rate which always decreases with partial screening. This is illustrated in figure 3.3, where the avalanche growth rate is plotted for a plasma with either neon or argon, resulting in a substantially higher growth rate than without impurities.

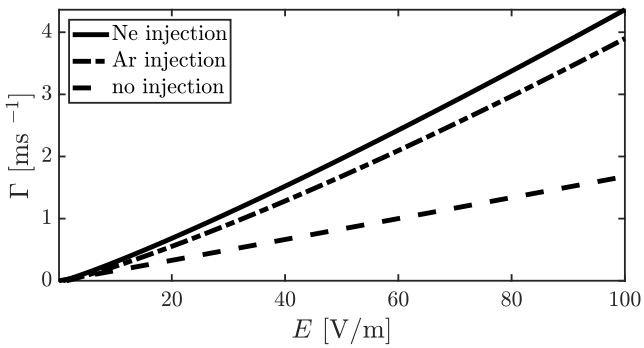

Figure 3.3: The avalanche growth rate (3.40) in a plasma with $T = 5\,\mathrm{eV}$ and $n_\mathrm{D} = 10^{20}\,\mathrm{m}^{-3}$, and an impurity injection $n_Z = n_\mathrm{D}$ of either doubly ionized neon (solid line) or triply ionized argon (dash-dotted line), which correspond to the equilibrium ionization states at the given temperature. For reference, the dashed line shows the growth rate without impurities.

3.3.3 Runaway-electron decay

The runaway beam that has formed during the current quench will eventually decay. This occurs when the runaway current becomes comparable to the Ohmic current, which reduces the induced electric field. Since runaway electrons experience fewer collisions than thermal particles, the current decay rate will be substantially slower than during the current

quench, and this phase is therefore sometimes referred to as the *runaway plateau*.

During the runaway plateau, the current decay rate is set by the effective critical electric field E_c^{eff} and the magnitude of the current (Breizman, 2014). This is because the avalanche growth rate is highly sensitive to the induced electric field, so an electric field that deviates too much from the effective critical electric field will cause a rapid growth or decay of runaway electrons, which will feed back on the current and the electric field. To prevent such rapid change in the current, $E \approx E_c^{\text{eff}}$ must hold if the runaway current is sufficiently large, and the zero-dimensional inductance equation (3.32) can be used to estimate the decay rate. Breizman (2014) used dimensional analysis to predict that a runaway current above 250 kA is required for $E \approx E_c^{\text{eff}}$ in a fully ionized plasma. Paper C performed a similar analysis for a partially ionized plasma with a large content of singly ionized argon ($n_{\text{e,Ar}}^{\text{tot}} \gg n_{\text{e,D}}$). Using equation (3.32) and the derived expression for E_c^{eff} from the same paper, we quantified the deviation from $E \approx E_c^{\text{eff}}$ and obtained $I_{\text{RE}} \gg 60\,\text{kA}$. This is sometimes fulfilled in medium-sized tokamaks and will generally hold in larger tokamaks such as ITER.

The runaway-electron decay phase is also where the runaway radiation losses are the most important. This is because both bremsstrahlung and synchrotron radiation are only effective at highly relativistic energies. When the electric field drops to near-critical values, the critical momentum (3.7) increases accordingly, which makes radiation reaction important also for the runaway generation rates, not only the runaway-electron distribution and maximum energy. Both bremsstrahlung and synchrotron radiation reaction losses are stronger in partially ionized plasmas; bremsstrahlung is directly enhanced by the effect of screening, whereas synchrotron radiation reaction becomes stronger due to the increased pitch-angle scattering rate. Both of these effects can increase the critical electric field by tens of percent, as we show in Paper C, which accordingly increases the electric field (and current decay rate) during the decay phase of the runaway beam.

Chapter 4

Reduced kinetic modeling of runaway electrons

The previous chapter outlined the basic momentum-space effects that govern runaway dynamics. While such analysis is suitable to develop an intuition, accurate modeling of experimental conditions do require a self-consistent evolution of the background plasma. As current computational resources do not allow a simultaneous treatment of the full kinetic problem together with the spatial dependence and the evolution of the electromagnetic fields, simplified models are needed. One possible approach is the use of reduced kinetic models, which were introduced in section 1.3. In this chapter, we discuss reduced kinetic modeling in more depth, and highlight our contributions to their improvement. We also discuss open questions and point out areas in which the reduced models need improvement before they can be reliably used for experimental validation and prediction. Finally, we highlight some possibilities for experimental validation of the kinetic theory.

4.1 Reduced kinetic models

In reduced kinetic models for runaway electrons, the momentum-space runaway dynamics are replaced by formulas for the steady-state runaway generation rates as a function of background parameters. These generation rates ideally provide accurate descriptions of the runaway

generation mechanisms described in section 3.3. To connect the obtained number density of runaway electrons to the current they carry, it is usually assumed that

$$j_{\mathrm{RE}} = e \int v_{\parallel} f_{\mathrm{RE}} d^3p \approx n_{\mathrm{RE}} e c, \tag{4.1}$$

i.e. the mean runaway parallel velocity is close to the speed of light, $\langle v_{\parallel} \rangle \approx c$. This current is then added to the Ohmic current produced by thermal electrons

$$j = j_{\Omega} + j_{\mathrm{RE}}, \tag{4.2}$$

which is coupled to the evolution of the electric field through the induction equation (3.19).

This reduced approach has been extensively used in previous studies. Most of the tools used, including the Chalmers-developed GO (see for example Fehér *et al.* (2011); Papp *et al.* (2013); Smith *et al.* (2006) and the more recent studies in Paper I and Paper K) as well as the work by Putvinski *et al.* (1997), Helander *et al.* (2002) and Martín-Solís *et al.* (2017), have a relatively simple model for the evolution of the electric field and the background plasma parameters. For example, the GO code solves the induction equation in a cylindrically symmetric plasma (3.20), with the possibility to account for plasma elongation (Paper I). The temperature is determined by considering the energy balance between Ohmic heating, line radiation, ionization, bremsstrahlung and collisions, and the ionization degree is determined by ionization and radiation rates taken from the ADAS database (Summers *et al.*, 2007). This means that GO neglects energy losses due to open flux surfaces, which should be justified if the ITER goal of 90 % radiated energy during the thermal quench is reached (see section 1.2). However, if the radiated target is not met, such MHD energy losses could be important. Therefore, the temperature in GO can alternatively be determined by assuming equilibrium between Ohmic heating and line radiation, which is similar to the model of Martín-Solís *et al.* (2017). As opposed to neglecting MHD losses, this temperature model can be considered to be a limit where MHD losses are large enough to quickly bring down the temperature to the sub-keV range, after which they are reduced so that the temperature evolution is governed by radiation and Ohmic heating.

Recently, more advanced tools for reduced kinetic runaway modeling have been developed. The software kit ASTRA-STRAHL (Linder *et al.*,

2020) is more accurate than previous tools as it accounts for the tokamak geometry and has a more accurate model for the evolution of the background plasma including the injected impurities. Further accuracy is obtained by using the runaway fluid module in the MHD solver JOREK (Bandaru *et al.*, 2019). With JOREK, it is possible to study the thermal quench dynamics in detail while following the runaway evolution. This includes an accurate determination of the temperature evolution, as well as the possibility to account for current diffusion when the field lines are open. Tools sush as JOREK however come at a significant computational expense, and it is not yet possible to resolve a full thermal quench without artificially increasing the plasma resistivity in the simulations.

Another recent development in the area of reduced kinetic models concerns the accuracy of the runaway generation rates. Above mentioned tools either neglected the effect of partial screening and the energy-dependent Coulomb logarithm, or used generalizations of the existing formulas which were not validated by kinetic simulations. In papers D and E, we addressed these shortcomings by obtaining more accurate generation rates due to the Dreicer and avalanche mechanisms, respectively. In both of these papers, we implemented the new generation rates in GO to evaluate their effect on the runaway dynamics as compared to the previously used expressions. In Paper D, we found that the more accurate avalanche growth rate (3.40) gave significantly larger predicted runaway currents in an ITER-like plasma. In Paper E, the improved Dreicer generation rate (described by equation (3.35)) reduced the runaway current in a GO simulation of a JET experiment, bringing it closer to the experimentally observed value. These results demonstrated that the effect of partial screening should be accounted for in runaway modeling. For this reason, the new generation rates have recently been implemented in ASTRA-STRAHL (Linder *et al.*, 2020).

4.2 Fluid-kinetic coupling

Although computationally more demanding, solving the coupled fluid-kinetic problem – formed by for example equations (2.29) and (3.20) – is possible with certain simplifications. With such a tool, it is possible to investigate in which regimes the reduced approach is expected to be accurate, and identify ways to improve the reduced models. It is also possible to obtain the distribution function as a function of radius.

One example of a coupled fluid-kinetic tool is GO+CODE. This tool was used in Papers I and K to assess the validity of runaway fluid modeling (see section 4.3.1), in Paper L to interpret synchrotron emission from a runaway distribution, and in Paper M to study runaway formation in the future SPARC tokamak.

GO+CODE couples the two codes by running CODE once for every time step and radial point in GO. In this way, the runaway current contribution is calculated so that

$$j_{\mathrm{RE}} = j - j_{\Omega} \tag{4.3}$$

instead of the estimate $j_{\mathrm{RE}} \approx n_{\mathrm{RE}} ec$, which is otherwise employed by GO. Furthermore, as CODE does not rely on the analytical steady-state generation rates to determine n_{RE}, the coupled tool can determine n_{RE} with higher accuracy than stand-alone GO. The GO+CODE tool was first outlined by Papp *et al.* (2015*b*), and improved by Vallhagen *et al.* (2019). Together with further improvements to the coupling scheme and the momentum grid used by CODE, this means that the computational cost of GO+CODE now allows for investigations of ITER-like plasmas, contrasting previously, when only simulations for smaller tokamaks were realistic.

In order to make GO+CODE computationally feasible, CODE only uses the test-particle collision operator described in section 2.2.1 with the partial screening corrections given in section 2.3. To compensate for the incorrect conductivity obtained with such an operator, the non-Ohmic current is modified before it is supplied to GO. By scanning over a wide range of effective charge and temperature, it was found that the conductivity with the test-particle collision operator is a Z_{eff}-dependent multiplicative factor of the fully relativistic conductivity σ_{BK} obtained by Braams & Karney (1989):

$$\sigma_{\mathrm{CODE,tp}} = g(Z_{\mathrm{eff}})\sigma_{\mathrm{BK}}. \tag{4.4}$$

In GO+CODE, the runaway current density j_{RE} is therefore determined by

$$j_{\mathrm{RE}} = j_{\mathrm{CODE,tp}} - \sigma_{\mathrm{CODE,tp}} E. \tag{4.5}$$

The same method can also be used when CODE is run with a self-consistent electric field. Then, the induced electric field is determined

from the current decay rate as in equation (3.32), with the current modified such that

$$j = j_{\text{CODE,tp}} + [1 - g(Z_{\text{eff}})]\,\sigma_{\text{BK}} E. \tag{4.6}$$

In partially ionized plasmas, the conductivity deviates somewhat from that obtained for the corresponding fully ionized plasma with the same effective charge, but the effect is small unless the ionization is significantly higher than the equilibrium state at a given temperature.

4.3 Validity of reduced kinetic models

For reduced kinetic models to be valid, it is important that the reduced model gives an accurate estimation of j_{RE}, at least in the phase where the runaway current gives a non-negligible contribution to the total current. To accomplish this, reduced models must also have an adequate description of transport, and effects of an inhomogeneous magnetic field can sometimes be important. These topics are discussed below.

4.3.1 Accuracy of runaway current prediction

To test whether reduced kinetic models can accurately estimate the runaway current, GO+CODE can advantageously be compared to GO, since they have the same model for the background plasma evolution. Initial investigations suggest that GO+CODE often gives higher runaway currents than pure GO simulations. As shown in Paper J by examining CODE results, the steady-state avalanche growth rate in equation (3.40) gives an accurate estimation of the instantaneous growth rate. This result has also been observed in GO+CODE simulations, which furthermore show that the assumption $\langle v_\parallel \rangle \approx c$ is valid for avalanche generation. This means that the final runaway current will be accurately estimated by reduced models, using the expression (4.1) in combination with the runaway generation rates to determine n_{RE}, if

(i) the number density of the seed population is sufficiently well described by the analytical formulas employed, and

(ii) the estimation $j = j_\Omega + n_{\text{RE}} ec$ is a good approximation.

Condition (i) is more easily fulfilled for a large avalanche multiplication factor N_{ava}, which was defined in equation (3.37). In that case, the final runaway current is only logarithmically sensitive to the initial seed population (see Paper I). Condition (ii) means that the seed population must be negligible, $j_{\mathrm{RE}} \ll j_{\Omega}$, until it has reached relativistic energies where $\langle v_{\parallel} \rangle \approx c$ is valid. As a small seed population leaves more room for avalanche generation, it is beneficial for reduced models that the runaway seed population is small but the plasma current sufficiently large that many avalanche multiplications can occur. In other words, reduced kinetic models can be expected to be more accurate in ITER-like scenarios than for small and medium-size tokamaks.

In scenarios with limited avalanche generation, there are indications that the reduced models perform poorly. For instance, if there is a significant runaway generation due to the Dreicer mechanism, so that $j_{\mathrm{RE}} \sim j_{\Omega}$, the feedback effect on the induced electric field will be inaccurate when the runaway electrons have not yet reached relativistic speeds. The situation is worse for hot-tail generation, which typically produces a low-energy runaway seed where, in addition, the analytical expressions of the number density (Smith & Verwichte, 2008) only have limited accuracy (Aleynikov & Breizman, 2017; Stahl *et al.*, 2016). These results imply that reduced kinetic models must go beyond the assumption $\langle v_{\parallel} \rangle \approx c$. As a first step, the runaway density could be complemented by a crude estimate of the mean parallel velocity.

Until reduced kinetic tools have been equipped with an estimation of $\langle v_{\parallel} \rangle$, the hot-tail seed current in particular can be vastly overpredicted in reduced models, and is therefore typically neglected. The effect of neglecting the hot-tail source was examined in Paper I and K by comparison to GO+CODE simulations, and it was found that the conversion from Ohmic to runaway current was substantially larger in the coupled simulations which included the hot-tail source. However, the GO+CODE simulations represent an upper limit on the hot-tail seed since they did not consider particle transport. This effect could potentially deconfine a large part of the hot-tail seed, as discussed in the following section.

4.3.2 Effect of transport on runaway-electron dynamics

Transport of runaway electrons is believed to have an appreciable effect on their dynamics. This is particularly important during the thermal

quench, where a large fraction of the hot-tail seed could be lost due to large induced magnetic perturbations and the resulting transport along open field lines. The runaway confinement during the thermal quench is highly uncertain and depends on the specific scenario as well as machine size; estimates of the seed survival fraction range from less than 0.1 % in the small Alcator C-Mod to almost 100 % in the large ITER, with JET and DIII-D in between at tens of percent (Izzo *et al.*, 2011; Sommariva *et al.*, 2017).

As the magnetic equilibrium is fixed in most of the reduced kinetic models, they cannot predict the time evolution of the magnetic perturbations or the spatial extent of the stochastic magnetic field line regions. Therefore, the fraction of lost hot-tail seed particles cannot be determined from first principles by for example GO, but requires computationally heavier approaches such as the nonlinear MHD tools JOREK (Czarny & Huysmans, 2008; Huysmans & Czarny, 2007), NIMROD (Sovinec *et al.*, 2004), or M3D-C (Breslau *et al.*, 2009). It is, however, possible to model some aspects of runaway transport even in simpler tools. For example, Boozer (2019) proposed a model for current evolution during breakup of magnetic surfaces based on a diffusion operator that conserves magnetic helicity. By varying the spatiotemporal extent of the stochastic magnetic field lines in this model, it would be possible to investigate the flattening of the radial current profile, and the change in the poloidal flux during this period should be excluded from the avalanche multiplication factor determined in section 3.3.2.

Several ways to include the effect of semi-static magnetic-field perturbations have also been proposed. A widely used diffusion-based model was developed by Rechester & Rosenbluth (1978), and the diffusion coefficient was further refined by Hauff & Jenko (2009), who based their model on simulations of turbulent transport. A radial diffusion model has been used by Helander *et al.* (2000) to study the effect of magnetic perturbations on avalanche generation, and the developed method can also be generalized to more accurate formulas for avalanche generation, such as the one developed in Paper D. However, several works point out that runaway transport induced by magnetic perturbations is not purely diffusive, but also has an advective component (Papp *et al.*, 2015*a*; Särkimäki *et al.*, 2016). Such an advection-diffusion model could be implemented in reduced kinetic tools, provided that the advection and diffusion coefficients are known.

Apart from magnetic perturbations, runaway electrons may also experience increased transport due to the so-called Ware pinch, which causes an inward convective particle flow. Recent work suggests that this effect can lead to a significantly different spatial distribution of runaway electrons (McDevitt *et al.*, 2019).

4.3.3 Effects of an inhomogeneous magnetic field

So far, we have discussed the case of cylindrically symmetrical plasmas. Such a model of runaway dynamics can correspond to, for example, the motion of particles close to the magnetic axis of a tokamak, where the inverse aspect ratio $\epsilon = r/R$ is small (r and R were defined in figure 3.2). A more general model can be obtained by considering a toroidally symmetric tokamak geometry, and noting that the the kinetic equation can be *gyro-averaged* over the helical gyro-motion around the magnetic field lines. This leaves the four phase-space variables $\{p_\parallel, p_\perp, r, \theta\}$ (where θ is again the toroidal angle), of which $p_\parallel, p_\perp$ are integrated over in fluid models. Such an equation is solved by for example the tool developed by McDevitt & Tang (2019).

The four-dimensional kinetic equation can be further simplified in two different limits. In a plasma with low collisionality, particles with sufficiently large magnetic moment $\mu_\mathrm{B} = p_\perp^2/(2mB)$ are *magnetically trapped* and make a "bouncing" motion in the poloidal angle, whereas other particles will circle the magnetic axis (Helander & Sigmar, 2005). In this case, the kinetic equation can be *orbit-averaged* over the poloidal angle, leaving a three-dimensional system in the variables $\{p_\parallel, p_\perp, r\}$. Such an equation can be solved by numerical tools such as LUKE (Decker & Peysson, 2004; Peysson & Decker, 2008; Peysson *et al.*, 2003) and CQL3D (Chiu *et al.*, 1998; Harvey *et al.*, 2000). This approach has been used to determine the effect of toroidicity on Dreicer and avalanche generation (Eriksson & Helander, 2003; Nilsson *et al.*, 2015; Rosenbluth & Putvinski, 1997), with order-unity reductions for both mechanisms at finite aspect ratio.

Conversely, at higher collisionality, particles on a trapped orbit can be collisionally de-trapped before completing an entire orbit, which causes the bounce-averaging approach to break down, and the runaway generation rate is determined by the local values of the background parameters. As the electric field often scales like $1/R$, McDevitt & Tang (2019) found

that the generation rate at high collisionality only depends weakly on the radial parameter, and may even increase slightly with r in contrast to the bounce-averaged case.

The parameter which determines the applicability of the bounce-averaging and the local limit is the collisionality, which is given by (Helander & Sigmar, 2005)

$$\nu_\star \equiv \frac{\nu_\mathrm{D}}{v}\frac{qR_0}{\epsilon^{3/2}}, \tag{4.7}$$

where R_0 is the on-axis major radius and q is the safety factor, which is the ratio of the average number of toroidal turns per poloidal turn of the magnetic field. For runaway dynamics, the energy-dependent parameter ν_D/v could be evaluated at the critical momentum p_c (McDevitt & Tang, 2019), which was defined in equation (3.7). A small value of $\nu_\star$ implies that the bounce-average approach is valid, whereas if $\nu_\star \gg 1$, runaway generation depends on the local electric field. If neither the small nor the large $\nu_\star$ limit is applicable, it is necessary to solve the four-dimensional kinetic equation, and it would be difficult to calculate runaway generation rates for use in reduced kinetic models.

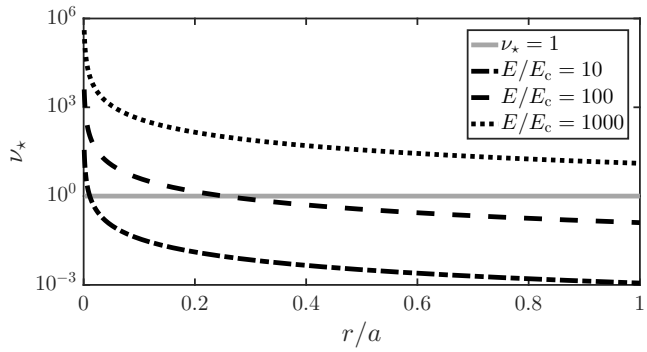

Figure 4.1: Collisionality as a function of radius normalized to the minor radius, at ITER-like, post-thermal-quench parameters: $n_\mathrm{e} = 10^{20}\,\mathrm{m}^{-3}$, $T = 10\,\mathrm{eV}$, $q = 2$, $Z_\mathrm{eff} = 1$, $a = 2\,\mathrm{m}$ and $R = 6\,\mathrm{m}$ (all plasma parameters are uniform in radius). The solid line shows the reference value $\nu_\star = 1$, and the remaining lines show three different electric-field strengths: $E/E_\mathrm{c} = 10$ (dash-dotted line), 100 (dashed line) and 1000 (dotted line).

As an example of its numerical value, $\nu_\star$ is evaluated for ITER-like, post-thermal-quench parameters in figure 4.1, assuming a fully ionized

plasma and $E \gg E_c$ (so that $p_c \approx 1/\sqrt{E/E_c} \ll 1$). The figure shows that $\nu_\star \gg 1$ for a large part of the parameter space studied, in particular when considering that both avalanche and Dreicer generation are most significant at larger electric fields, and that the electric field often peaks close to the magnetic axis. This indicates that the local theory accurately describes runaway dynamics in certain post-disruption plasmas, and that the avalanche generation rates calculated in Papers D and E are accurate without further corrections. This picture is largely supported by computing the spatiotemporal evolution of $\nu_\star$ for simulations with GO, and comparing to where the majority of runaway generation took place. However, the analysis also showed that the bounce-averaged limit is more appropriate if the post-disruption temperature is higher and there is no impurity content to increase ν_D. A thorough investigation to determine the applicability of the the local versus the bounce average limits has yet to be conducted, and this remains one of the open areas for progress in advancing reduced kinetic modeling.

4.4 Experimental validation of models

Future tokamak devices require a high disruption mitigation success rate. It is therefore crucial to have experimentally validated models which are capable of predicting the outcome of the envisaged mitigation schemes, but runaway modeling has not yet reached a level of maturity at which it consistently gives agreement with experiment. Moreover, only a few quantities related to runaway dynamics are experimentally accessible. A further complication is that experimental measurements during disruption conditions are challenging, which results in large uncertainties in the background plasma parameters such as the plasma composition, density and temperature. Consequently, it is difficult to validate models such as those developed in this thesis, but there are nevertheless some possibilities.

Massive material injection – especially involving pellets – is particularly difficult to both measure and model. Even if the effect of a given impurity species on runaway dynamics is now understood (partially via the work in this thesis), it is more difficult to determine the ionization states and spatio-temporal distribution of the impurities. One aspect that is usually not accounted for in modelling is ionization caused by runaway electrons. Recent work indicates that a large runaway population can in-

crease the ionization level of the impurities substantially (Garland *et al.*, 2020), but the runaway population is likely too small during most of the runaway formation process for large effects. Regarding the impurity deposition, a difficulty with massive gas injection is understanding the gas assimilation in the machine, while shattered pellet injection allows somewhat simpler modeling of material penetration, but requires modeling of the complicated ablation process. Therefore, studies of massive gas (Nardon *et al.*, 2017) and shattered pellet injection (Hoelzl *et al.*, 2020; Kim *et al.*, 2019), usually aim for a qualitative rather than quantitative agreement with experiments.

For runaway electrons, the plasma current is arguably the most reliable of the relevant experimental observables. In the late stage of the current quench, it can often be assumed that most of the current is carried by runaway electrons, which implies that the plasma current can give valuable information about not only the current quench time but also the runaway plateau current and the runaway current decay rate. Runaway simulations typically overpredict the runaway plateau current, which is often attributed to the rudimentary description of plasma losses, although it is difficult to rule out experimental uncertainties or other shortcomings of the model (Papp *et al.*, 2013).

An aspect of the runaway current evolution which shows better agreement with theory is the decay rate. The decay rate is particularly suitable for experimental validation, since it is one of few quantities relatively straightforward to both predict from kinetic theory and diagnose experimentally – as discussed in section 3.3.3, the decay rate is set by the effective critical electric field if the plasma current is large. Such a comparison was recently conducted by Papp *et al.* (2019), who found that the decay rate was consistent with the prediction $E \approx E_{\mathrm{c}}^{\mathrm{eff}}$ as calculated by the formula in Paper C.

Another piece of information in the plasma current evolution is the plasma current spike, which usually accompanies the onset of the disruption (Boozer, 2019). This current spike occurs due to magnetic reconnection, and can be used to diagnose the breakup of magnetic flux surfaces which is important for runaway transport as well as current evolution (Boozer, 2019). In MHD simulations to date, the current spike is typically too small, which may be caused by the artificially increased resistivity typically used to reduce the computational demands (Nardon *et al.*, 2017). If the disagreement can be solved in the future, it could be

possible to extract a simplified description of these MHD effects from the simulations, which could then be used to improve the reduced kinetic models.

Apart from the plasma current, the most important diagnostics for runaway electrons are detectors of synchrotron and bremsstrahlung emission (Breizman *et al.*, 2019), which both have high sensitivity at relativistic energies (Hollmann *et al.*, 2015*a*). This emission could in principle be used to reconstruct the runaway-electron distribution function, as opposed to the runaway current which saturates when the parallel velocity approaches the speed of light. However, this inverse problem is usually ill-posed, implying that some assumptions are required to enable inversion of the spectrum or image from synchrotron or bremsstrahlung emission. A number of studies have inferred information about the runaway electron energy, pitch-angle or radial distriubution from either bremsstrahlung emission (Hoppe *et al.*, 2018*a*; Paz-Soldan *et al.*, 2017; Shevelev *et al.*, 2013), synchrotron images (Hoppe *et al.*, 2018*b*; Tinguely *et al.*, 2018) or a combination of synchrotron and bremsstrahlung spectra (Hollmann *et al.*, 2015*a*). In comparisons with kinetic models, these studies typically found that theory predicts higher energies than are inferred from experiments, which is often attributed to losses that are neglected in the models.

A drawback with both radiation diagnostics and the plasma current is that they cannot quantify the runaway electron density during the runaway generation phase. It is therefore difficult to experimentally validate runaway generation rates, which is key to understand discrepancies between models and measurements of radiation or the runaway plateau current. There have however been some efforts also in this direction. For example, Hollmann *et al.* (2011*b*) measured the growth rate of a pre-formed runaway beam when applying an external electric field. They found that the measured growth rate was lower than predicted by theory, but a resolution to the inconsistency was recently proposed via the influence of kinetic instabilities (Paz-Soldan *et al.*, 2019). However, since the applied electric fields were modest in comparison to those which can be induced during a disruption, it was only possible to probe the physics near the critical electric field. Another example is the study by Hollmann *et al.* (2016), who estimated the runaway-electron seed from the enhancement of pellet ablation by non-thermal electrons in DIII-D experiments. Although the error bars are large, the estimated seed cur-

rent is consistent with reaching the observed runaway plateau current after avalanche multiplication according to equation (3.39), but existing models of hot-tail and Dreicer deviated by more than an order of magnitude from the experimental value.

Some of the studies mentioned in the previous paragraph were conducted in partially ionized plasmas, and thus an accurate analysis should include the effect of partial screening. Possibly, similar studies with varying plasma composition could offer the best validation opportunities for the model developed through this thesis. In particular, if it were possible to increase the accuracy of the runaway seed measurement, it would allow for an experimental validation of the avalanche growth rate derived in Paper D. Such a validation would be more reliable in a large, high-current tokamak, which can have a larger avalanche multiplication and induced electric field, and is presumably less sensitive to transport and kinetic instabilities.

Chapter 5

Concluding remarks

Since runaway electrons have the potential to severely damage tokamaks, developing the understanding of their behavior is an active area in tokamak fusion research. In particular, it is crucial to be able to model scenarios with impurity injection, which is the envisaged mitigation method in the upcoming ITER experiment. In such scenarios, the impurities are partially ionized, meaning that the atomic nuclei are partially screened by bound electrons when interacting with runaway electrons. This thesis focuses on deriving a collision operator for a partially ionized plasma, and investigates several aspects of runaway-electron dynamics in such plasmas.

In the appended papers, we have systematically investigated the effect of partial screening on the kinetics of fast electrons. By combining analytical derivations and numerical simulations using the tool CODE, we have built up a qualitative as well as quantitative understanding of runaway-electron dynamics in partially ionized plasmas, and contributed to more accurate reduced kinetic models. The present chapter summarizes the main findings of these papers. We then put these results into a broader context by discussing their implications for runaway mitigation and a few possible directions in which the present work can be continued.

5.1 Summary of papers

Papers A and B were focused on the derivation of the collision operator and identifying the effect of partial screening on various aspects of runaway dynamics. In Paper A, we presented the collision operator for partially ionized plasmas, which includes a quantum-mechanical description of both elastic collisions with the partially screened nuclei, and of inelastic collisions with the bound electrons. By matching the scattering rates with bound electrons to the classical low-energy limit, we obtained a self-contained collision operator formulated in terms of modified collision frequencies. This operator can therefore be straightforwardly implemented in numerical tools, as has been done recently in CODE (Paper A) as well as the works by del Castillo-Negrete *et al.* (2018) and McDevitt *et al.* (2019). The analytical results indicated that a detailed model of the fast-electron dynamics requires the use of the collision operator for partially ionized plasmas. We found that neither complete screening (i.e. treating the ion as a particle carrying the net charge) nor no screening (treating the bound electrons as if they were free) give good approximations of the collision frequencies; complete screening gives a significant underestimation, whereas no screening provides a considerable overestimation of the collision frequencies. This picture was supported by kinetic simulations using CODE, which showed significant changes to the shape of the runaway distribution.

While Paper A introduced the collision operator and presented the initial studies, the main purpose of Paper B was to present the full derivation of the collision operator and investigate several subtle issues that arose. Specifically, we compared the Fokker–Planck collision operator with the more advanced Boltzmann operator. We found that the runaway distributions produced with the collision operator for partially ionized plasmas and the full Boltzmann operator had negligible differences in all key runaway parameters such as runaway current and density, although the synchrotron spectrum was somewhat different in shape at large electric fields. Consequently, the generalized collision operator introduced is adequate for most purposes of runaway-electron studies in tokamaks.

The collision operator for partially ionized plasmas contains a parameter which can be interpreted as a length scale related to the ion radius. While Paper A presented these constants for a few ionization states, Paper B calculated the constants for a wide range of ion species and

compared them to previous models. We found that a previously used simplified model without any free parameters (Kirillov *et al.*, 1975) gave acceptable accuracy for use in the collision operator. This will facilitate future modeling as it reduces the need for computationally heavy density functional theory simulations.

Some concrete results found in Papers A and Paper B were that partial screening can increase the runaway decay rate and avalanche growth rate, but decreases the Dreicer generation rate. This means that the enhanced collision rates with partial screening can be both beneficial and detrimental; enhanced damping and reduced Dreicer generation are positive for runaway mitigation while the increased avalanche growth is negative. Papers C, D and E were devoted to investigate, quantify and develop models for each of these three effects.

In Paper C, the collision operator for partially ionized plasmas was applied to determine the critical electric field. The critical electric field is not only important fundamentally since it is the threshold field above which runaway generation can occur, but also because it sets the decay rate of a runaway beam in an inductive device, such as a high-current tokamak. In Paper C, we employed the approximation of fast pitch-angle dynamics (Aleynikov & Breizman, 2015; Lehtinen *et al.*, 1999) to calculate the critical electric field. This resulted in an analytical formula for the effective critical field. This formula was demonstrated to agree within a few percent with numerical results from CODE, which was extended to include partial screening in the bremsstrahlung operator and the avalanche source. The effective critical field was shown to be significantly enhanced compared to previous estimations, and it was elevated by tens of percent by bremsstrahlung and synchrotron radiation losses. Additionally, we used CODE to verify the prediction that the induced electric field is close to the effective critical electric field during runaway in high-current inductive devices. This prediction appears to be consistent with recent experiments, as discussed in section 4.4.

Paper D analyzed avalanche generation in partially ionized plasmas. We generalized the Rosenbluth & Putvinski (1997) calculation by including the effect of partial screening as derived in Paper A. As in the original calculation, we solved the kinetic equation in several parameter regimes, including the behavior near the critical electric field from Paper C. By interpolating between the different results, we obtained a semi-analytical expression for the avalanche growth rate. This expression was success-

fully benchmarked against kinetic simulations with CODE. We found that the steady-state growth rate at high electric fields was enhanced by the presence of partially screened nuclei. This is because the bound electrons lead to a stronger avalanche source which dominates over the increased collisional damping of runaway electrons.

To explore the effect in various regimes of parameter space, we determined the avalanche multiplication factor of a trace runaway seed when the electric-field evolution follows that in section 3.2.2, and integrated the avalanche growth rate in time. To isolate the effect of impurities on the kinetic dynamics, the temperature was fixed for all densities, although experimental predictions would certainly require a self-consistent calculation, accounting for the effect of impurity density on the thermal quench dynamics. In the classical calculation of the avalanche multiplication factor, detailed in section 3.3.2, most of the parametric dependences cancel out, which results in a robust prediction of the avalanche multiplication factor: it only depends on the change in the poloidal flux, as long as the induced electric field significantly exceeds the critical electric field. This exact cancellation does not arise with partially ionized impurities since the growth rate is no longer directly proportional to the electric field even at large induced electric fields. This means that the potential multiplication of a runaway seed varies substantially across parameter space. As we showed in Paper D, this can increase the avalanche multiplication factor substantially. To further demonstrate the effect, we implemented the growth rate in the runaway fluid tool GO, and calculated the final runaway current assuming a fixed runaway seed density. We found that the new growth rate substantially increases the runaway current if a large amount of impurities is injected to the plasma. This highlights the need to update the avalanche growth rate in reduced kinetic models. These results also indicate that the negative effects of massive material injection could outweigh the positive effects when it comes to runaway formation.

Finally, Paper E developed a tool that determines the Dreicer generation rate in partially ionized plasmas. With partially ionized impurities, the Dreicer generation rate can decrease by several orders of magnitude, since the increased friction and pitch-angle scattering shifts the balance between electric-field acceleration and damping to higher energies where there are fewer particles to be runaway accelerated. Since the Dreicer generation rate is exponentially sensitive to the thermal properties of

the plasma and the input data depends on many free parameters, we used a neural network approach, which is suitable to fit complicated, high-dimensional results. The resulting neural network was trained on CODE data, and subsequently implemented in GO. We demonstrated the use of the neural network by investigating a scenario resembling an experiment in the largest existing tokamak JET. In this scenario, we found that the decreased Dreicer generation was nearly canceled by increased avalanche generation due to partial screening. This conclusion does however not hold universally; in ITER for example, avalanche generation is more prominent and the seed generation is dominated by non-Dreicer sources (probably hot-tail during the non-nuclear phase), which implies that partial screening should increase runaway generation. On the other hand, a net decrease in runaway current could be expected in smaller, Dreicer-dominated tokamaks.

In summary, we found that an accurate treatment of partial screening can have large and rather non-trivial effects on runaway-electron momentum-space dynamics. These results take us one step forward in understanding how runaway electrons can be affected by material injection. Through Papers C-E, we also contribute to the development of reduced kinetic models. How these can be used, as well as other steps toward a model capable of reliable experimental predictions, is discussed in the following section.

5.2 Outlook

In this thesis, we address the runaway interaction with an assumed background density of impurities, but we do not consider how the material was injected into and ionized by the plasma. In order to make predictions for disruptions in tokamaks, these pieces need to be combined into a single model, which also includes the evolution of the other background plasma properties (Aleynikov & Breizman, 2017; Fehér *et al.*, 2011; Gál *et al.*, 2008; Knoepfel & Spong, 1979).

With this thesis, we contribute to the development of such a model by providing more accurate expressions for runaway generation through the avalanche and Dreicer mechanisms. These have already been implemented in GO (Paper K) as well as the reduced kinetic tool ASTRA-STRAHL (Linder *et al.*, 2020). However, the range of applicability of re-

duced kinetic models remains unclear. To map the parameter space and identify possible improvements of reduced kinetic models would therefore be a highly relevant application of CODE and GO+CODE. One example of an already known area of improvement is the description of hot-tail, as the assumption of relativistic electron velocities tends to drastically overestimate runaway production.

One of the scenarios to investigate with more advanced reduced models is massive material injection. For instance, it would be valuable to validate our results in Paper D obtained by GO, which has a simplified description of the background plasma evolution. These results showed that impurity injection is not necessarily helpful for runaway mitigation in ITER as it increases avalanche generation. This would imply that the optimal mitigation scheme for the heat load and force during the thermal and current quench could aggravate the runaway problem. If integrated simulations support the results obtained with this idealized model, it is unclear whether there are any injection parameters that can simultaneously meet all the mitigation targets; perhaps some of the targets need to be relaxed in order to find a suitable compromise between different sources of damage. For example, decreasing the amount of injected material would make it more difficult to reach the targets on radiated energy fraction and current quench length, but may possibly prevent excessive runaway generation. In order to find the optimal injection scheme, reliable and accurate simulations are needed – and the results obtained through this thesis can give some guidance in this respect.

An interesting finding with partial screening is that there does not necessarily exist a density above which runaway generation is avoided. It was previously believed that sufficient material injection could increase the critical electric field until runaway formation could be entirely prevented. However, we found that higher impurity or deuterium densities decrease the temperature which, in turn, increase the induced electric field and reduces the ionization (see Paper K). This effect seems to dominate over the increase in the effective critical electric field, indicating that with partial screening, runaway generation can be substantial up to experimentally unattainable densities.

Before the reduced kinetic models can make reliable predictions, additional pieces are needed. Most notably, the representation of the transport of runaway electrons must be improved, in particular to determine

the fraction of runaway seed electrons that are lost during the thermal quench. A better understanding of kinetic instabilities is also desirable. At least in some scenarios, wave-particle instabilities may be needed to explain experimental results (Liu *et al.*, 2018; Paz-Soldan *et al.*, 2019), although it is uncertain whether these effects can be important during disruptions in large tokamaks.

Runaway research is a high priority, since it is of the utmost importance for the success of the fusion program that runaway electron damage can be prevented in future devices. This thesis is one step toward experimental validation of runaway modeling, and reliable predictions for future devices such as ITER. In the longer term, it may contribute to robust runaway mitigation schemes which are a milestone in the development of operational fusion power plants.

References

Aleynikov, P. & Breizman, B. N. (2015), *Theory of two threshold fields for relativistic runaway electrons*, Phys. Rev. Lett. **114** 155001, doi: 10.1103/PhysRevLett.114.155001.

Aleynikov, P. & Breizman, B. N. (2017), *Generation of runaway electrons during the thermal quench in tokamaks*, Nuclear Fusion **57** 046009, doi: 10.1088/1741-4326/aa5895.

Bandaru, V., Hoelzl, M., Artola, F. J., Papp, G. & Huijsmans, G. T. A. (2019), *Simulating the nonlinear interaction of relativistic electrons and tokamak plasma instabilities: Implementation and validation of a fluid model*, Phys. Rev. E **99** 063317, doi: 10.1103/PhysRevE.99.063317.

Bellan, P. M. (2004), *Fundamentals of plasma physics*, Cambridge University Press.

Berger, M. J., Inokuti, M., Anderson, H. H., Bichsel, H., Dennis, J. A., Powers, D., Seltzer, S. M. & Turner, J. E. (1984), *4. Selection of mean excitation energies for elements*, Journal of the International Commission on Radiation Units and Measurements **os19** 22, doi: 10.1093/jicru/os19.2.15.

Bethe, H. (1930), *Zur theorie des durchgangs schneller korpuskularstrahlen durch materie*, Annalen der Physik **397** 325, doi: 10.1002/andp.19303970303, (in German).

Boozer, A. H. (2005), *Physics of magnetically confined plasmas*, Rev. Mod. Phys. **76** 1071, doi: 10.1103/RevModPhys.76.1071.

Boozer, A. H. (2018), *Pivotal issues on relativistic electrons in ITER*, Nuclear Fusion **58** 036006, doi: 10.1088/1741-4326/aaa1db.

Boozer, A. H. (2019), *Magnetic surface loss and electron runaway*, Plasma Physics and Controlled Fusion **61** 024002, doi: 10.1088/1361-6587/aaf293.

Braams, B. J. & Karney, C. F. F. (1989), *Conductivity of a relativistic plasma*, Physics of Fluids B: Plasma Physics **1** 1355, doi: 10.1063/1.858966.

Breizman, B. N. (2014), *Marginal stability model for the decay of runaway electron current*, Nuclear Fusion **54** 072002, doi: 10.1088/0029-5515/54/7/072002.

Breizman, B. & Aleynikov, P. (2017), *Kinetics of relativistic runaway electrons*, Nuclear Fusion **57** 125002, doi: 10.1088/1741-4326/aa8c3f.

Breizman, B. N., Aleynikov, P., Hollmann, E. M. & Lehnen, M. (2019), *Physics of runaway electrons in tokamaks*, Nuclear Fusion **59** 083001, doi: 10.1088/1741-4326/ab1822.

Breslau, J., Ferraro, N. & Jardin, S. (2009), *Some properties of the M3D-C1 form of the three-dimensional magnetohydrodynamics equations*, Physics of Plasmas **16** 092503, doi: 10.1063/1.3224035, https://doi.org/10.1063/1.3224035.

Cabal, H., Lechón, Y., Bustreo, C., Gracceva, F., Biberacher, M., Ward, D., Dongiovanni, D. & Grohnheit, P. (2017), *Fusion power in a future low carbon global electricity system*, Energy Strategy Reviews **15** 1, doi: 10.1016/j.esr.2016.11.002.

Cannas, B., Fanni, A., Pautasso, G., Sias, G. & Sonato, P. (2010), *An adaptive real-time disruption predictor for ASDEX Upgrade*, Nuclear Fusion **50** 075004, doi: 10.1088/0029-5515/50/7/075004.

del Castillo-Negrete, D., Carbajal, L., Spong, D. & Izzo, V. (2018), *Numerical simulation of runaway electrons: 3-D effects on synchrotron radiation and impurity-based runaway current dissipation*, Physics of Plasmas **25** 056104, doi: 10.1063/1.5018747.

CEA (2016), *A short history of magnetic fusion*, http://www-fusion-magnetique.cea.fr/gb/fusion/histoire/site_historique.htm, accessed 2019-12-03.

Cercignani, C. & Kremer, G. M. (2002), *Relativistic boltzmann equation*, in *The Relativistic Boltzmann Equation: Theory and Applications*, Springer.

Chiu, S., Rosenbluth, M., Harvey, R. & Chan, V. (1998), *Fokker-planck simulations mylb of knock-on electron runaway avalanche and bursts in tokamaks*, Nuclear Fusion **38** 1711, doi: 10.1088/0029-5515/38/11/309.

Commaux, N. *et al.* (2016), *First demonstration of rapid shutdown using neon shattered pellet injection for thermal quench mitigation on DIII-D*, Nuclear Fusion **56** 046007, doi: 10.1088/0029-5515/56/4/046007.

Connor, J. & Hastie, R. (1975), *Relativistic limitations on runaway electrons*, Nuclear Fusion **15** 415.

Czarny, O. & Huysmans, G. (2008), *Bézier surfaces and finite elements for mhd simulations*, Journal of Computational Physics **227** 7423 , ISSN 0021-9991, doi: https://doi.org/10.1016/j.jcp.2008.04.001.

Decker, J. & Peysson, Y. (2004), *DKE: A fast numerical solver for the 3D drift kinetic equation*, Tech. Rep. EUR-CEA-FC-1736, Euratom-CEA.

Decker, J., Hirvijoki, E., Embréus, O., Peysson, Y., Stahl, A., Pusztai, I. & Fülöp, T. (2016), *Numerical characterization of bump formation in the runaway electron tail*, Plasma Physics and Controlled Fusion **58** 025016, doi: 10.1088/0741-3335/58/2/025016.

Dreicer, H. (1959), *Electron and ion runaway in a fully ionized gas. I*, Phys. Rev. **115** 238, doi: 10.1103/PhysRev.115.238.

Dreicer, H. (1960), *Electron and ion runaway in a fully ionized gas. II*, Phys. Rev. **117** 329, doi: 10.1103/PhysRev.117.329.

Dwyer, J. R. (2007), *Relativistic breakdown in planetary atmospheres*, Physics of Plasmas **14** 042901, doi: 10.1063/1.2709652.

Embréus, O., Stahl, A. & Fülöp, T. (2016), *Effect of bremsstrahlung radiation emission on fast electrons in plasmas*, New Journal of Physics **18** 093023, doi: 10.1088/1367-2630/18/9/093023.

Embréus, O., Stahl, A. & Fülöp, T. (2018), *On the relativistic large-angle electron collision operator for runaway avalanches in plasmas*, Journal of Plasma Physics **84** 905840102, doi: 10.1017/S002237781700099X.

Eriksson, L.-G. & Helander, P. (2003), *Simulation of runaway electrons during tokamak disruptions*, Computer Physics Communications **154** 175, doi: 10.1016/S0010-4655(03)00293-5.

Esposito, B., Martín-Solís, J. R., Poli, F. M., Mier, J. A., Sánchez, R. & Panaccione, L. (2003), *Dynamics of high energy runaway electrons in the Frascati Tokamak Upgrade*, Physics of Plasmas **10** 2350, doi: 10.1063/1.1574328.

Fehér, T., Smith, H. M., Fülöp, T. & Gál, K. (2011), *Simulation of runaway electron generation during plasma shutdown by impurity injection in ITER*, Plasma Physics and Controlled Fusion **53** 035014, doi: 10.1088/0741-3335/53/3/035014.

Freidberg, J. P. (2007), *Plasma physics and fusion energy*, Cambridge University Press.

Fülöp, T. & Newton, S. (2014), *Alfvénic instabilities driven by runaways in fusion plasmas*, Physics of Plasmas **21** 080702, doi: 10.1063/1.4894098.

Gál, K., Fehér, T., Smith, H., Fülöp, T. & Helander, P. (2008), *Runaway electron generation during plasma shutdown by killer pellet injection*, Plasma Physics and Controlled Fusion **50** 055006, doi: 10.1088/0741-3335/50/5/055006.

Garbet, X. & Deutsch, C. (1986), *Mean excitation energies for arbitrarily stripped ions in dense and hot matter*, Europhysics Letters (EPL) **2** 761, doi: 10.1209/0295-5075/2/10/004.

Garland, N. A., Chung, H.-K., Fontes, C. J., Zammit, M. C., Colgan, J., Elder, T., McDevitt, C. J., Wildey, T. M. & Tang, X.-Z. (2020), *Impact of a minority relativistic electron tail interacting with a thermal plasma containing high-atomic-number impurities*, Physics of Plasmas **27** 040702, doi: 10.1063/5.0003638.

Granetz, R. S. *et al.* (2014), *An ITPA joint experiment to study runaway electron generation and suppression*, Physics of Plasmas **21** 072506, doi: 10.1063/1.4886802.

Guan, X., Qin, H. & Fisch, N. J. (2010), *Phase-space dynamics of runaway electrons in tokamaks*, Physics of Plasmas **17** 092502, doi: 10.1063/1.3476268.

Harvey, R. W., Chan, V. S., Chiu, S. C., Evans, T. E., Rosenbluth, M. N. & Whyte, D. G. (2000), *Runaway electron production in DIII-D killer pellet experiments, calculated with the CQL3D/KPRAD model*, Physics of Plasmas **7** 4590, doi: 10.1063/1.1312816.

Hauff, T. & Jenko, F. (2009), *Runaway electron transport via tokamak microturbulence*, Physics of Plasmas **16** 102308, doi: 10.1063/1.3243494.

Heitler, W. (1954), *The quantum theory of radiation*, Courier Corporation.

Helander, P. & Sigmar, D. (2005), *Collisional Transport in Magnetized Plasmas*, Cambridge University Press, ISBN 9780521020985.

Helander, P., Eriksson, L.-G. & Andersson, F. (2000), *Suppression of runaway electron avalanches by radial diffusion*, Physics of Plasmas **7** 4106.

Helander, P., Eriksson, L.-G. & Andersson, F. (2002), *Runaway acceleration during magnetic reconnection in tokamaks*, Plasma Physics and Controlled Fusion **44** B247, doi: 10.1088/0741-3335/44/12B/318.

Helander, P., Smith, H., Fülöp, T. & Eriksson, L.-G. (2004), *Electron kinetics in a cooling plasma*, Physics of Plasmas **11** 5704, doi: 10.1063/1.1812759.

Hender, T. *et al.* (2007), *Chapter 3: MHD stability, operational limits and disruptions*, Nuclear Fusion **47** S128, doi: 10.1088/0029-5515/47/6/S03.

Hirvijoki, E., Decker, J., Brizard, A. J. & Embréus, O. (2015*a*), *Guiding-centre transformation of the radiation–reaction force in a non-uniform magnetic field*, Journal of Plasma Physics **81** 475810504, doi: 10.1017/S0022377815000744.

Hirvijoki, E., Pusztai, I., Decker, J., Embréus, O., Stahl, A. & Fülöp, T. (2015*b*), *Radiation reaction induced non-monotonic fea-*

tures in runaway electron distributions, Journal of Plasma Physics **81** 475810502, DOI: 10.1017/S0022377815000513/.

Hoelzl, M., Hu, D., Nardon, E. & Huijsmans, G. T. A. (2020), *First predictive simulations for deuterium shattered pellet injection in ASDEX Upgrade*, Physics of Plasmas **27** 022510, DOI: 10.1063/1.5133099.

Hollmann, E. M. *et al.* (2011*a*), *Plasma–surface interactions during tokamak disruptions and rapid shutdowns*, Journal of Nuclear Materials **415** S27, DOI: 10.1016/j.jnucmat.2010.10.009.

Hollmann, E. M. *et al.* (2011*b*), *Effect of applied toroidal electric field on the growth/decay of plateau-phase runaway electron currents in DIII-D*, Nuclear Fusion **51** 103026, DOI: 10.1088/0029-5515/51/10/103026.

Hollmann, E. M. *et al.* (2013), *Control and dissipation of runaway electron beams created during rapid shutdown experiments in DIII-D*, Nuclear Fusion **53** 083004, DOI: 10.1088/0029-5515/53/8/083004.

Hollmann, E. M. *et al.* (2015*a*), *Measurement of runaway electron energy distribution function during high-Z gas injection into runaway electron plateaus in DIII-D*, Physics of Plasmas **22** 056108, DOI: 10.1063/1.4921149.

Hollmann, E. M. *et al.* (2015*b*), *Status of research toward the ITER disruption mitigation system*, Physics of Plasmas **22** 021802, DOI: 10.1063/1.4901251.

Hollmann, E. M. *et al.* (2016), *Use of Ar pellet ablation rate to estimate initial runaway electron seed population in DIII-D rapid shutdown experiments*, Nuclear Fusion **57** 016008, DOI: 10.1088/0029-5515/57/1/016008.

Holman, G. D. (1985), *Acceleration of runaway electrons and Joule heating in solar flares*, Astrophysical Journal **293** 584, DOI: 10.1086/163263.

Hoppe, M., Embréus, O., Paz-Soldan, C., Moyer, R. & Fülöp, T. (2018*a*), *Interpretation of runaway electron synchrotron and bremsstrahlung images*, Nuclear Fusion **58** 082001, DOI: 10.1088/1741-4326/aaae15.

Hoppe, M., Embréus, O., Tinguely, R., Granetz, R., Stahl, A. & Fülöp, T. (2018*b*), *SOFT: a synthetic synchrotron diagnostic for runaway electrons*, Nuclear Fusion **58** 026032, doi: 10.1088/1741-4326/aa9abb.

Huysmans, G. & Czarny, O. (2007), *MHD stability in x-point geometry: simulation of ELMs*, Nuclear Fusion **47** 659, doi: 10.1088/0029-5515/47/7/016.

Izzo, V. A. *et al.* (2011), *Runaway electron confinement modelling for rapid shutdown scenarios in DIII-D, Alcator C-Mod and ITER*, Nuclear Fusion **51** 063032, doi: 10.1088/0029-5515/51/6/063032.

Jackson, J. D. (1999), *Classical electrodynamics*, Wiley.

Jayakumar, R., Fleischmann, H. & Zweben, S. (1993), *Collisional avalanche exponentiation of runaway electrons in electrified plasmas*, Physics Letters A **172** 447.

Kates-Harbeck, J., Svyatkovskiy, A. & Tang, W. (2019), *Predicting disruptive instabilities in controlled fusion plasmas through deep learning*, Nature **568** 526, doi: 10.1038/s41586-019-1116-4.

Kim, C. C., Liu, Y., Parks, P. B., Lao, L. L., Lehnen, M. & Loarte, A. (2019), *Shattered pellet injection simulations with NIMROD*, Physics of Plasmas **26** 042510, doi: 10.1063/1.5088814.

Kirillov, V. D., Trubnikov, B. A. & Trushin, S. A. (1975), *Role of impurities in anomalous plasma resistance*, Soviet Journal of Plasma Physics **1** 117.

Knoepfel, H. & Spong, D. (1979), *Runaway electrons in toroidal discharges*, Nuclear Fusion **19** 785, doi: 10.1088/0029-5515/19/6/008.

Konovalov, S. *et al.* (2016), *Assessment of the runaway electron energy dissipation in ITER*, in *26th IAEA Fusion Energy Conference – IAEA CN-234*, TH/7–1.

Kruskal, M. & Bernstein, I. B. (1962), *Princeton Plasma Physics Lab*, Report no. MATT-Q-20 172.

Lamoureux, M. & Avdonina, N. (1997), *Bremsstrahlung in hot plasmas with partially ionized atoms*, Phys. Rev. E **55** 912, doi: 10.1103/PhysRevE.55.912.

Landau, L. D. & Lifshitz, E. M. (1958), *Quantum mechanics: non-relativistic theory*, Pergamon Press.

Landreman, M., Stahl, A. & Fülöp, T. (2014), *Numerical calculation of the runaway electron distribution function and associated synchrotron emission*, Computer Physics Communications **185** 847, doi: 10.1016/j.cpc.2013.12.004.

Lehnen, M. *et al.* (2015), *Disruptions in ITER and strategies for their control and mitigation*, Journal of Nuclear Materials **463** 39, doi: 10.1016/j.jnucmat.2014.10.075.

Lehtinen, N. G., Bell, T. F. & Inan, U. S. (1999), *Monte Carlo simulation of runaway MeV electron breakdown with application to red sprites and terrestrial gamma ray flashes*, Journal of Geophysical Research: Space Physics **104** 24699, doi: 10.1029/1999JA900335.

Linder, O., Fable, E., Jenko, F., Papp, G. & Pautasso, G. (2020), *Self-consistent modeling of runaway electron generation in massive gas injection scenarios in ASDEX Upgrade*, Nuclear Fusion (accepted), doi: 10.1088/1741-4326/ab9dcf.

Liu, C., Hirvijoki, E., Fu, G.-Y., Brennan, D. P., Bhattacharjee, A. & Paz-Soldan, C. (2018), *Role of kinetic instability in runaway-electron avalanches and elevated critical electric fields*, Phys. Rev. Lett. **120** 265001, doi: 10.1103/PhysRevLett.120.265001.

Martín-Solís, J. R., Loarte, A. & Lehnen, M. (2015), *Runaway electron dynamics in tokamak plasmas with high impurity content*, Physics of Plasmas **22** 092512, doi: 10.1063/1.4931166.

Martín-Solís, J., Loarte, A. & Lehnen, M. (2017), *Formation and termination of runaway beams in ITER disruptions*, Nuclear Fusion **57** 066025, doi: 10.1088/1741-4326/aa6939.

Matthews, G. F. *et al.* (2016), *Melt damage to the JET ITER-like wall and divertor*, Physica Scripta **T167** 014070, doi: 10.1088/0031-8949/t167/1/014070.

McDevitt, C. J. & Tang, X.-Z. (2019), *Runaway electron generation in axisymmetric tokamak geometry*, EPL (Europhysics Letters) **127** 45001, doi: 10.1209/0295-5075/127/45001.

McDevitt, C. J., Guo, Z. & Tang, X.-Z. (2019), *Spatial transport of runaway electrons in axisymmetric tokamak plasmas*, Plasma Physics and Controlled Fusion **61** 024004, doi: 10.1088/1361-6587/aaf4d1.

Mehlhorn, T. A. (1981), *A finite material temperature model for ion energy deposition in ion-driven inertial confinement fusion targets*, Journal of Applied Physics **52** 6522, doi: 10.1063/1.328602.

Montgomery, D. & Tidman, D. (1964), *Plasma Kinetic Theory*, McGraw-Hill advanced physics monograph series, McGraw-Hill.

Mosher, D. (1975), *Interactions of relativistic electron beams with high atomic-number plasmas*, Physics of Fluids **18** 846, doi: 10.1063/1.861219.

Nardon, E. *et al.* (2016), *On the mechanisms governing gas penetration into a tokamak plasma during a massive gas injection*, Nuclear Fusion **57** 016027, doi: 10.1088/0029-5515/57/1/016027.

Nardon, E., Fil, A., Hoelzl, M., Huijsmans, G. & JET contributors (2017), *Progress in understanding disruptions triggered by massive gas injection via 3d non-linear MHD modelling with JOREK*, Plasma Physics and Controlled Fusion **59** 014006, doi: 10.1088/0741-3335/59/1/014006.

Nilsson, E., Decker, J., Peysson, Y., Granetz, R. S., Saint-Laurent, F. & Vlainic, M. (2015), *Kinetic modelling of runaway electron avalanches in tokamak plasmas*, Plasma Physics and Controlled Fusion **57** 095006, doi: 10.1088/0741-3335/57/9/095006.

Papp, G., Drevlak, M., Fülöp, T. & Pokol, G. I. (2012), *The effect of resonant magnetic perturbations on runaway electron transport in ITER*, Plasma Phys. Controlled Fusion **54** 125008, doi: 10.1088/0741-3335/54/12/125008.

Papp, G. *et al.* (2013), *The effect of ITER-like wall on runaway electron generation in JET*, Nuclear Fusion **53** 123017, doi: 10.1088/0029-5515/53/12/123017.

Papp, G., Drevlak, M., Pokol, G. I. & Fülöp, T. (2015*a*), *Energetic electron transport in the presence of magnetic perturbations in magnetically confined plasmas*, Journal of Plasma Physics **81** 475810503, doi: 10.1017/S0022377815000537.

Papp, G., Stahl, A., Drevlak, M., Fülöp, T., Lauber, P. W. & Pokol, G. (2015*b*), *Towards self-consistent runaway electron modeling*, Europhysics Conference Abstracts **39E** P1.173, http://ocs.ciemat.es/EPS2015PAP/pdf/P1.173.pdf.

Papp, G. *et al.* (2019), *The effect of high-Z material injection on runaway electron dynamics*, 46th EPS Conference on Plasma Physics I4.105, http://ocs.ciemat.es/EPS2019ABS/pdf/I4.105.pdf.

Paszke, A. *et al.* (2019), *PyTorch: an imperative style, high-performance deep learning library*, in *Advances in Neural Information Processing Systems 32*, 8024, Curran Associates, Inc.

Pautasso, G. *et al.* (2018), *The ITER disruption mitigation trigger: developing its preliminary design*, Nuclear Fusion **58** 036011, doi: 10.1088/1741-4326/aaa137.

Paz-Soldan, C. *et al.* (2017), *Spatiotemporal evolution of runaway electron momentum distributions in tokamaks*, Phys. Rev. Lett. **118** 255002, doi: 10.1103/PhysRevLett.118.255002.

Paz-Soldan, C. *et al.* (2019), *Recent DIII-D advances in runaway electron measurement and model validation*, Nuclear Fusion **59** 066025, doi: 10.1088/1741-4326/ab1769.

Peysson, Y. & Decker, J. (2008), *Calculation of RF current drive in tokamaks*, AIP Conference Proceedings **1069** 176, doi: 10.1063/1.3033701.

Peysson, Y., Decker, J. & Harvey, R. W. (2003), *Advanced 3-D electron Fokker–Planck transport calculations*, AIP Conference Proceedings **694** 495, doi: 10.1063/1.1638086.

Pike, O. J. & Rose, S. J. (2014), *Dynamical friction in a relativistic plasma*, Phys. Rev. E **89** 053107, doi: 10.1103/PhysRevE.89.053107.

Pokol, G. I., Kómár, A., Budai, A., Stahl, A. & Fülöp, T. (2014), *Quasi-linear analysis of the extraordinary electron wave destabilized by runaway electrons*, Physics of Plasmas **21** 102503, doi: 10.1063/1.4895513.

Putvinski, S., Fujisawa, N., Post, D., Putvinskaya, N., Rosenbluth, M. & Wesley, J. (1997), *Impurity fueling to terminate*

tokamak discharges, Journal of Nuclear Materials **241** 316, DOI: 10.1016/S0022-3115(97)80056-6.

Rattá, G., Vega, J., Murari, A., Vagliasindi, G., Johnson, M., de Vries, P. & JET EFDA contributors (2010), *An advanced disruption predictor for JET tested in a simulated real-time environment*, Nuclear Fusion **50** 025005, DOI: 10.1088/0029-5515/50/2/025005.

Rechester, A. B. & Rosenbluth, M. N. (1978), *Electron heat transport in a tokamak with destroyed magnetic surfaces*, Phys. Rev. Lett. **40** 38, DOI: 10.1103/PhysRevLett.40.38.

Reux, C. *et al.* (2015), *Runaway electron beam generation and mitigation during disruptions at JET-ILW*, Nuclear Fusion **55** 093013, DOI: 10.1088/0029-5515/55/9/093013.

Rosenbluth, M. & Putvinski, S. (1997), *Theory for avalanche of runaway electrons in tokamaks*, Nuclear Fusion **37** 1355, DOI: 10.1088/0029-5515/37/10/I03.

Rosenbluth, M. N., MacDonald, W. M. & Judd, D. L. (1957), *Fokker-planck equation for an inverse-square force*, Phys. Rev. **107** 1, DOI: 10.1103/PhysRev.107.1.

Särkimäki, K., Hirvijoki, E., Decker, J., Varje, J. & Kurki-Suonio, T. (2016), *An advection-diffusion model for cross-field runaway electron transport in perturbed magnetic fields*, Plasma Physics and Controlled Fusion **58** 125017, DOI: 10.1088/0741-3335/58/12/125017.

Sauer, S. P., Oddershede, J. & Sabin, J. R. (2015), *Chapter three - the mean excitation energy of atomic ions*, in *Concepts of Mathematical Physics in Chemistry: A Tribute to Frank E. Harris - Part A*, vol. 71 of *Advances in Quantum Chemistry*, 29, Academic Press, DOI: 10.1016/bs.aiq.2015.02.001.

Shevelev, A. *et al.* (2013), *Reconstruction of distribution functions of fast ions and runaway electrons in fusion plasmas using gamma-ray spectrometry with applications to ITER*, Nuclear Fusion **53** 123004, DOI: 10.1088/0029-5515/53/12/123004.

Smith, H. M. & Verwichte, E. (2008), *Hot tail runaway electron generation in tokamak disruptions*, Physics of Plasmas **15** 072502, doi: 10.1063/1.2949692.

Smith, H., Helander, P., Eriksson, L.-G. & Fülöp, T. (2005), *Runaway electron generation in a cooling plasma*, Physics of Plasmas **12** 122505, doi: 10.1063/1.2148966.

Smith, H., Helander, P., Eriksson, L.-G., Anderson, D., Lisak, M. & Andersson, F. (2006), *Runaway electrons and the evolution of the plasma current in tokamak disruptions*, Physics of Plasmas **13** 102502, doi: 10.1063/1.2358110.

Smith, H. M., Boozer, A. H. & Helander, P. (2013), *Passive runaway electron suppression in tokamak disruptions*, Physics of Plasmas **20** 072505, doi: 10.1063/1.4813255.

Sokolov, Y. (1979), *"Multiplication" of accelerated electrons in a tokamak*, JETP Letters **29** 218.

Solodov, A. A. & Betti, R. (2008), *Stopping power and range of energetic electrons in dense plasmas of fast-ignition fusion targets*, Physics of Plasmas **15** 042707, doi: 10.1063/1.2903890.

Sommariva, C., Nardon, E., Beyer, P., Hoelzl, M., Huijsmans, G., van Vugt, D. & JET contributors (2017), *Test particles dynamics in the JOREK 3d non-linear MHD code and application to electron transport in a disruption simulation*, Nuclear Fusion **58** 016043, doi: 10.1088/1741-4326/aa95cd.

Sovinec, C. *et al.* (2004), *Nonlinear magnetohydrodynamics with high-order finite elements*, J. Comp. Phys. **195** 355.

Stahl, A., Hirvijoki, E., Decker, J., Embréus, O. & Fülöp, T. (2015), *Effective critical electric field for runaway electron generation*, Physical Review Letters **114** 115002, doi: 10.1103/PhysRevLett.114.115002.

Stahl, A., Embréus, O., Papp, G., Landreman, M. & Fülöp, T. (2016), *Kinetic modelling of runaway electrons in dynamic scenarios*, Nuclear Fusion **56** 112009, doi: 10.1088/0029-5515/56/11/112009.

Stahl, A., Landreman, M., Embréus, O. & Fülöp, T. (2017), *NORSE: A solver for the relativistic non-linear Fokker–Planck equa-*

tion for electrons in a homogeneous plasma, Computer Physics Communications **212** 279, DOI: 10.1016/j.cpc.2016.10.024.

Summers, H. P., O'Mullane, M. G., Whiteford, A. D., Badnell, N. R. & Loch, S. D. (2007), *ADAS: Atomic data, modelling and analysis for fusion*, AIP Conference Proceedings **901** 239, DOI: 10.1063/1.2727374.

Tinguely, R. A., Granetz, R. S., Hoppe, M. & Embréus, O. (2018), *Spatiotemporal evolution of runaway electrons from synchrotron images in Alcator C-Mod*, Plasma Physics and Controlled Fusion **60** 124001, DOI: 10.1088/1361-6587/aae6ba.

Tong, D. (2012), *Kinetic theory*, http://damtp.cam.ac.uk/user/tong/statphys.html, accessed 2019-12-03.

Vallhagen, O., Johansson, A., Unnerfelt, L., Hermansson, E., Hansson, J. & Eriksson, O. (2019), *Numerical modelling of runaway electrons in suddenly cooling fusion plasmas*, https://ft.nephy.chalmers.se/files/publications/5dc8145f41680.pdf.

de Vries, P. & Gribov, Y. (2018), *Size matters: ITER breakdown and plasma initiation revisited*, Europhysics Conference Abstracts **42A** O3.109, http://ocs.ciemat.es/EPS2018PAP/pdf/O3.109.pdf.

de Vries, P., Johnson, M., Alper, B., Buratti, P., Hender, T., Koslowski, H., Riccardo, V. & JET-EFDA contributors (2011), *Survey of disruption causes at JET*, Nuclear Fusion **51** 053018, DOI: 0029-5515/51/5/053018.

Wesson, J. (2011), *Tokamaks*, Oxford University Press, 4 ed.

Wesson, J. *et al.* (1989), *Disruptions in JET*, Nuclear Fusion **29** 641, DOI: 10.1088/0029-5515/29/4/009.

Wroblewski, D., Jahns, G. & Leuer, J. (1997), *Tokamak disruption alarm based on a neural network model of the high-beta limit*, Nuclear Fusion **37** 725, DOI: 10.1088/0029-5515/37/6/i02.

Zhogolev, V. & Konovalov, S. (2014), *Characteristics of interaction of energetic electrons with heavy impurity ions in a tokamak plasma*, VANT *or* Problems of Atomic Sci. and Tech. series Thermonuclear Fusion **37** 71, (in Russian).